The relation among the ring current, subauroral polarization stream, and the geospace plume: MAGE Simulation of the March 31 2001 Super Storm

Shanshan Bao[1], Wenbin Wang[2], Kareem Sorathia[3], Viacheslav G. Merkin[3], Frank R. Toffoletto[1], Dong Lin[4], Kevin H Pham[4], Jeffrey Garretson[5], Michael Wiltberger[6], John G. Lyon[7], and Adam Michael[8]

[1]Rice University
[2]HAO/NCAR
[3]The Johns Hopkins University Applied Physics Laboratory
[4]National Center for Atmospheric Research
[5]Johns Hopkins Applied Physics Lab
[6]National Center for Atmospheric Research (UCAR)
[7]Dartmouth College
[8]The John Hopkins Applied Physics Laboratory

August 4, 2023

Abstract

The geospace plume, referring to the combined processes of the plasmaspheric and the ionospheric storm-enhanced density (SED)/total electron content (TEC) plumes, is one of the unique features of geomagnetic storms. The apparent spatial overlap and joint temporal evolution between the plasmaspheric plume and the equatorial mapping of the SED/TEC plume indicate strong magnetospheric-ionospheric coupling. However, a systematic modeling study of the factors contributing to geospace plume development has not yet been performed due to the lack of a sufficiently comprehensive model including all the relevant physical processes. In this paper, we present a numerical simulation of the geospace plume in the March 31, 2001 storm using the Multiscale Atmosphere Geospace Environment model. The simulation reproduces the observed linkage of the two plumes, which, we interpret as a result of both being driven by the electric field that maps between the magnetosphere and the ionosphere. The model predicts two velocity channels of sunward plasma drift at different latitudes in the dusk sector during the storm main phase, which are identified as the sub-auroral polarization stream (SAPS) and the convection return flow, respectively. The SAPS is responsible for the erosion of the plasmasphere plume and contributes to the ionospheric TEC depletion in the midlatitude trough region. We further find the spatial distributions of the magnetospheric ring current ions and electrons, determined by a delicate balance of the energy-dependent gradient/curvature drifts and the E´B drifts, are crucial to sustain the SAPS electric field that shapes the geospace plume throughout the storm main phase.

The relation among the ring current, subauroral polarization stream, and the geospace plume: MAGE Simulation of the March 31 2001 Super Storm

Shanshan Bao[1], Wenbin Wang[2], Kareem Sorathia[3], Viacheslav Merkin[3], Frank Toffoletto[1], Dong Lin[2], Kevin Pham[2], Jeffrey Garretson[3], Michael Wiltberger[2], John Lyon[4] and Adam Michael[3]

[1]Department of Physics and Astronomy, Rice University, Houston TX

[2]High Altitude Observatory, National Center for Atmospheric Research, Boulder CO

[3]Applied Physics Laboratory, Johns Hopkins University, Laurel MD

[4]Department of Physics and Astronomy, Dartmouth College, Hanover NH

Corresponding author: Shanshan Bao (shanshan.bao@rice.edu)

Key Points:

- The first whole geospace simulation to demonstrate coherent storm-time evolution of plasmaspheric and total electron content (TEC) plumes.
- The model demonstrates plasmasphere erosion and TEC depletion by the subauroral polarization streams (SAPS).
- SAPS is sustained by magnetospheric ion and electron distributions formed by a delicate balance of energy-dependent and **E**×**B** drifts.

Abstract

The geospace plume, referring to the combined processes of the plasmaspheric and the ionospheric storm-enhanced density (SED)/total electron content (TEC) plumes, is one of the unique features of geomagnetic storms. The apparent spatial overlap and joint temporal evolution between the plasmaspheric plume and the equatorial mapping of the SED/TEC plume indicate strong magnetospheric-ionospheric coupling. However, a systematic modeling study of the factors contributing to geospace plume development has not yet been performed due to the lack of a sufficiently comprehensive model including all the relevant physical processes. In this paper, we present a numerical simulation of the geospace plume in the March 31, 2001 storm using the Multiscale Atmosphere Geospace Environment model. The simulation reproduces the observed linkage of the two plumes, which, we interpret as a result of both being driven by the electric field that maps between the magnetosphere and the ionosphere. The model predicts two velocity channels of sunward plasma drift at different latitudes in the dusk sector during the storm main phase, which are identified as the sub-auroral polarization stream (SAPS) and the convection return flow, respectively. The SAPS is responsible for the erosion of the plasmasphere plume and contributes to the ionospheric TEC depletion in the midlatitude trough region. We further find the spatial distributions of the magnetospheric ring current ions and electrons, determined by a delicate balance of the energy-dependent gradient/curvature drifts and the E×B drifts, are crucial to sustain the SAPS electric field that shapes the geospace plume throughout the storm main phase.

1 Introduction

During geomagnetically active times, multiscale dynamic processes are triggered throughout the magnetosphere, the ionosphere and the thermosphere in response to the solar wind driving. Once the global magnetospheric convection initiates, the ring current starts to accumulate, reshaping the global structure of the magnetosphere and establishing a distinctive dynamic storm-time pattern of the electromagnetic field and plasmas. The Imager for Magnetopause-to Aurora Global Exploration (IMAGE) satellite observed the dynamic evolution of the cold (~1eV) and dense (~ 10^4/cc) plasmasphere (Lemaire et al., 1998) and the sunward extension of a plume-like high density structure from the dusk edge of the plasmasphere (the “drainage plume”) through the EUV images (Burch et al., 2001; Sandel et al., 2001; Goldstein, 2004; Goldstein & Sandel, 2005). The IMAGE satellite also detected, through the high-energy neutral atom (HENA) images, that the spatial distribution of the partial ring current roughly complements the shape of the plasmapause (Pulkkinen et al., 2005; Goldstein, 2007). In the ionosphere, the storm-time electron density enhancement at low to midlatitudes in the day and dusk sectors is a prominent feature known as a “positive storm effect” (Liu et al., 2016; Fagundes et al., 2016). Furthermore, a plume-like high total electron content (TEC) structure extends from the positive storm effect region in the noon-to-dusk sector toward higher latitudes and into the polar cap, which is commonly observed by incoherent scatter radars, ground-based Global Positioning System (GPS) measurements and near-Earth satellites (e.g., Foster, 1993; Zou et al., 2013, 2014; Foster et al., 2020). The term “geospace plume” has been used to refer to the coupled, jointly evolving high plasma density structures including the plasmaspheric drainage plume and the storm-enhanced density (SED)/TEC plume in the ionosphere (Foster et al., 2020). Foster et al. (2002) first pointed out the “linkage” between the plasmaspheric plume and the ionospheric SED/TEC plume by comparing the IMAGE EUV plasmasphere image and the equatorial mapping of the GPS TEC map. They noted that the co-location of the plumes indicates strong magnetosphere-ionosphere (MI) coupling. Further observations show that the sub-auroral polarization stream (SAPS), a latitudinally narrow large plasma drift channel in the sub-auroral ionosphere in the dusk-to-midnight sector (Foster & Burke, 2002), may play an important role in shaping the dusk edge of the plasmasphere and further depleting the middle latitude electron density trough in the ionosphere. In other words, the SAPS electric field maps across the plasmapause on the dusk side causing strong westward ion transport and contributes to the formation of the ionospheric electron density trough which is co-located with the SAPS channel (Foster & Burke, 2002; Foster, 2002; Foster et al., 2007, 2014; Zou et al., 2021).

Numerical simulations of the geospace plume system have been conducted along with the observational studies. Goldstein et al. (2003, 2005, 2014) used cold test particles at the plasmapause that were driven by empirical convection and an ad-hoc SAPS electric potential to track the plasmasphere evolution. They found that the SAPS electric field is crucial in order to reproduce the storm-time, dusk-side structures of the plasmasphere, such as the plasmapause radius and the plasmaspheric plume. The first 3D simulation of the plasmasphere was conducted using the SAMI3 model that was driven by an empirical electrostatic potential (Huba & Krall, 2013). The study found that the simulated plasmasphere evolves from a toroidal symmetric shape into a contracted size with a development of a plume-like structure after the storm. The Thermosphere Ionosphere Electrodynamics General Circulation Model (TIEGCM) (Richmond et al., 1992; Qian et al., 2014) has been extensively used to investigate thermosphere-ionospheric response to geospace disturbances and SAPS. For example, C. H. Lin et al. (2005) used the TIEGCM with the $\mathbf{E}\times\mathbf{B}$ drift derived from satellite measurements of the ion velocity to study the relative importance of winds and electric field for low and midlatitude electron density enhancements. Wang et al. (2012) and Lu et al. (2020) used a synthetic SAPS electric field model to investigate the response of neutral winds, SED plume and traveling ionospheric disturbances to SAPS. SAMI3 coupled with the Rice Convection Model (RCM) of the inner magnetosphere was used to simulate the evolution of the ionosphere-plasmasphere system and demonstrated the linkage between the plamaspheric plume and the mapped SED/TEC plume during a geomagnetic storm (Huba & Sazykin, 2014, 2017).

In recent years, magnetosphere-ionosphere-thermosphere (M-I-T) coupled models have been developed and used to simulate SAPS (Raeder et al., 2016; Lin et al., 2019, 2021, 2022). These studies showed that the coupled geospace models can capture the complex interactions and feedback loops in the M-I-T system and reproduce the distinctive features of SAPS in observations. Yet, such coupled models have not yet been used to study the geospace plume. Most of the previous modeling studies simulated the plasmaspheric plume and the ionospheric SED/TEC plume separately, precluding studies that would elucidate the physics underlining the linkage between the two plumes. The use of ad-hoc or empirical SAPS electric field instead of self-consistent, physics-based SAPS modeling prevents an investigation of the magnetosphere-ionospheric coupling processes involved, where the coupled processes of the ring current buildup, the Region-2 current generation and the electron precipitation could play important roles in the generation of SAPS (Lin et al., 2021, 2022) and the plume dynamics. SAMI3-RCM simulation (Huba & Sazykin, 2014, 2017) had the advantage of a common electromagnetic field driving both ionospheric and magnetospheric plumes in the closed-field-line region, but it lacked a physics-based representation of high-latitude dynamics coupled to the rest of the simulation domain and an outer-magnetosphere model that can provide the ring current model with storm-time plasma injections at its boundary (Bao et al., 2021; Cramer et al., 2017; De Zeeuw et al., 2004; Lin et al., 2021; Pembroke et al., 2012).

In this study, we use such a coupled M-I-T model to gain a comprehensive understanding of the geospace plume evolution during storm-times. We address three science questions: (1) What is the cause of the linkage between the plamaspheric plume and the ionospheric SED/TEC plume? (2) What specific processes are important for shaping the geospace plume? (3) What is the relation between the ring current build-up and the geospace plume development? For this purpose, we employ the Multiscale Atmosphere-Geospace Environment (MAGE) model (Lin et al., 2021, 2022; Pham et al., 2022) to simulate the multiscale dynamics throughout the outer and inner magnetosphere, the ionosphere and the thermosphere to determine the relevant correlations and potential causal relationships. The coupled whole geospace model requires a number of key components. First is the global magnetospheric MHD model that can capture both global and inner magnetospheric dynamics such as large-scale storm-time magnetospheric convection and particle gradient/curvature drifts and provide self-consistent dynamic magnetic field configuration along with the associated current system. A coupled thermosphere-ionospheric model is also needed to not only self-consistently evolve the upper atmospheric neutral species but also simulate ionospheric electron densities, and provide ionospheric conductance to solve the current continuity equation for the global ionospheric electrostatic potential. Finally, the model must include the coupling of FACs, particle precipitation, ionospheric conductance, and ionospheric electric field to ensure feedback and self-consistency within the entire geospace system.

2 The MAGE model

The MAGE model used in this study provides a comprehensive and self-consistent description of multiscale physical processes in the different domains of geospace. The current version of MAGE (1.0) couples the global magnetosphere, the inner magnetosphere, the ionosphere and the thermosphere (Lin et al., 2021, 2022; Pham et al., 2022). As shown in Figure 1, the global magnetospheric MHD model, Grid Agnostic MHD with Extended Research Applications (GAMERA) model (Zhang et al., 2019; Sorathia et al., 2020) solves the single-fluid MHD equations and passes FACs to the ionosphere potential solver, and the RE-developed Magnetosphere-Ionosphere Coupler/Solver (REMIX) which is a rewrite of the Magnetosphere-Ionosphere Coupler/Solver (MIX) code (Merkin & Lyon, 2010). REMIX solves the electric potential for both hemispheres. The GAMERA plasma moments and electromagnetic field are passed to the Rice Convection Model (RCM), the inner magnetosphere ring current model (Toffoletto et al., 2003), to evolve the drifting plasma distribution in the form of multiple-fluids with different energy invariants. The plasmasphere is modeled as a zero-energy proton channel in RCM and follows the $\mathbf{E}\times\mathbf{B}$ drift including corotation. The plasmasphere is initialized with a 2D density profile as a function of the Kp index modified from the 1D Gallagher model (Gallagher et al., 2000). The total plasma density and pressure are fed back to the GAMERA model. There are also two kinds of electron precipitation simulated by the current MAGE model: the RCM-computed diffuse electron precipitation, i.e., pitch-angle scattered electrons falling into the loss cone (Wolf, 1983; Bao, 2019), and the GAMERA-computed mono-energetic electron precipitation accelerated by field-aligned potential drops (Zhang et al., 2015). The electron precipitation and the electric potential are used as input to the TIEGCM that calculates the density, temperature and transport of electrons, ions, and neutrals. The electron precipitation, along with the solar EUV radiation, produces ionization in the ionosphere and the ionospheric conductivity.

Two important physical processes are not yet included in MAGE and therefore are not addressed in this study. The first is a physics-based representation of the plasmaspheric refilling process. In the current version of MAGE, we model the plasmasphere inside the inner-magnetosphere model, RCM, with a simple empirical refilling model being used, whereas the ionospheric electron density is solved separately in a coupled thermosphere-ionospheric model, TIEGCM. Specifically, in this study, the refilling model is in fact turned off to isolate the effects of electrodynamic coupling and investigate whether the linkage of the two plumes still exists without mass exchange. Plasmasphere refilling is a slow process (~ days) compared with the storm-time plasmaspheric density changes (~ hours) (Lawrence et al., 1999; Denton et al., 2012; Krall et al., 2014) and the exclusion of the refilling should not fundamentally change the storm-time plasmaspheric dynamics.

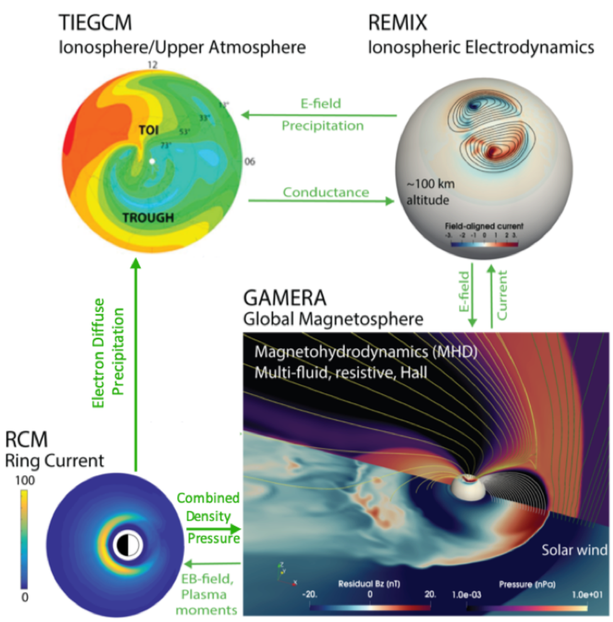

Figure 1. Diagram of the MAGE components and their coupling in this study.

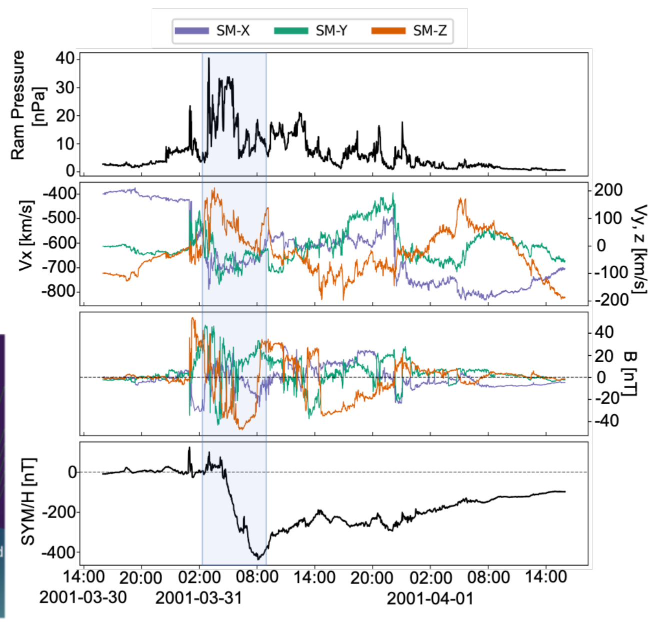

Figure 2. Solar wind dynamic pressure and velocity (top two panels), IMF components (third panel), and the SYM-H index (bottom panel) during the March 31, 2001, super storm. Data source: CDAWeb/NASA

2.1 Simulation Setup

The event studied in the paper is the super storm that occurred on March 31, 2001. The super storm was a result of a coronal mass ejection event that caused the SYM/H index to reach -400 nT. Figure 2 shows the solar wind profile, including, from top to bottom, the dynamic ram pressure, the solar wind velocity components, the interplanetary magnetic field (IMF) components, and the SYM/H index, extracted from the NASA/GSFC's OMNI dataset through CDAWeb. There are two periods of southward (SW) IMF, the first, 03:00~08:00UT 03-31-2001, which was followed by a period of northward IMF, and the second, 15:00~22:00UT. The simulation covered the entire storm, but our analysis focuses mostly on the geospace plume development in the first period of the southward IMF (highlighted in Figure 2 in blue shade).

In this work, we use the so called ‘Quad’ resolution for GAMERA, which corresponds to 96, 96, and 128 grid cells in radial, meridional and azimuthal directions (the spherical axis of the grid is aligned with the Solar Magnetic (SM) x-axis). The non-uniform 3D grid is much denser in the inner magnetosphere region with its inner boundary set at 1.5R_E. The REMIX 2D grid is 1°×1° in longitude and latitude with a low latitude boundary at 35° magnetic latitude (MLAT). The RCM 2D physical grid is 1°×1/3° in longitude and latitude and for the energy grid, it uses 1 energy channel for the plasmasphere, 29 energy channels for the electrons and 84 energy channels for the protons. Oxygen channels are not used in this study. GAMERA, REMIX and RCM grids are defined in the SM coordinates. The TIEGCM 3D grid covers the entire globe and is defined in the geographic coordinates. Its resolution is 1.25°×1.25° in longitude and latitude and it has 57 levels of vertical pressure grid (1/4 scale height resolution), ranging from ~97 km to approximately 900 km. The coupling exchange interval between GAMERA and REMIX is 5 s, while for GAMERA and RCM, the exchange interval is 15 s and for REMIX and TIEGCM, it is 5 s. The MAGE simulation starts at 16:00 UT, March 30, 2001 and lasts for 48 hours.

3. Overview of the simulation results

The evolution of the geospace plume is shown in Figure 3 through different stages of the storm (specifically for the 1st period of the southward IMF in Figure 2). The entire process of geospace plume development is demonstrated in Movies S1 and S2. In Figure 3(a1)-(a5) (the first row) and (d1)-(d5) (the fourth row), we map the relevant processes onto the magnetic equatorial plane defined as the surface of minimum magnetic field. The plasmapause as the 100/cc iso-surface of the cold proton density. The colored areas are within the closed-field-line region and the blanked areas are for the open-field-line region. The electric potential ϕ plotted in the equatorial plane is a combination of the ionospheric electrostatic potential ϕ_I and the corotation potential ϕ_c, defined as

$$\phi = \phi_I + \phi_c \tag{1}$$

$$\phi_c = -\frac{\omega_E B_0 R_E^3}{r} \tag{2}$$

where r is the radial distance; ω_E is the angular speed of the Earth’s rotation; B_0 is the strength of the Earth’s dipole moment; R_E is the radius of the Earth (Toffoletto et al., 2003). The contours of the electric potential represent the streamlines of the plasma **E**×**B** drift flow. Here, the ionospheric electrostatic potential ϕ_I is calculated by REMIX and shown in Figure 3(b1)-(b5) (the second row). The ionospheric potential calculated by TIEGCM is shown in Figure(c1)-(c5) (the third row), where it uses the electric potential from REMIX in the high latitude region (MLAT > 60) and solves for global ionospheric potential including the neutral wind dynamo. All the ionospheric plots in this paper are for the northern hemisphere.

At the pre-storm stage (Figures 3(a1)-(d1), the first column), both the FACs and the ionospheric electric potential are weak. The co-rotation electric field dominates and drives the plasmasphere co-rotate with the Earth, with the plasmapause around 3.5~4R_E (bottom row, Figure 3(d1) The ionospheric TEC peaks near 20 MLAT with a value of ~140 TECu and has a higher value (>50TECu) in the noon-to-dusk sector from low- to midlatitude than in the midnight-to-dawn sector.

Around 02:30~04:30UT, 03-31-2001, the impact of the CME event arrives at Earth, with an evident increase in the ram pressure and fluctuations in the IMF (Figure 2) causing the storm initial phase. By the end of the initial phase (Figure 3(a2)-(d2), the second column) the solar wind driving has caused the formation of the Region-1 current, while the Region-2 current is still relatively weak. The two-cell convection pattern in the electric potential starts to establish and this initiates global-scale sunward convection on the nights side (Figure 3(b2)), although the ring current has not yet developed (Figure 3(a2)). From the extent of the dashed contour lines of the potential in Figure 3(d2), we can see that a plume-like structure began to emerge in the plasmasphere as well as in the middle-high latitude ionosphere. Specifically, the plasmasphere starts to expand sunward and a finger-like structure (a plasmaspheric “finger”) starts to develop at the dusk edge of the plasmapause (heavy line in Figure 3(d2)). We will briefly discuss its cause in Section 4.2.1.

During the early main phase (Figure 3(a3)-(d3), the third column), the FACs and the ionospheric convection electric fields become stronger (Figure 3(b3)). The Region-2 current is enhanced due to a substantial ring current pressure accumulation (Figure 3(a3)). The peak of the TEC has moved to 30 MLAT and a TEC plume occurs with ~70TECu and expands toward the polar cap from 45 MLAT to 75 MLAT near 14 MLT driven by the dusk-cell of the convection (Figure 3(c3)). The plasmaspheric plume has formed, with the plasmasphere finger merged into its main body (Figure 3(d3)). The shape of the plasmaspheric plume maintains approximate dawn-dusk symmetry about the noon-midnight line in the equatorial plane.

In the late main phase (Figure 3(a4)-(d4), the fourth column), the strength of the ring current reaches its maximum. Due to the westward drifting of the ion population, the ring current pressure distribution is skewed toward pre-midnight (Figure 3(a4)). The FACs become much more intense (Figure 3(b4)) causing stronger central convection electric field that enhances the ionospheric-poleward/equatorial-sunward expansion of the geospace plume (Figure 3(b4), (c4) and (d4)). The high TEC region due to the positive storm effect extends from 30 MLAT to 45 MLAT and 60 MLAT in the ionosphere (Figure 3(c4)) and it becomes the center of the TEC plume on the equatorial plane (Figure 3(d4)). Meanwhile, the two-cell convection pattern is skewed clockwise, where the dusk-side pair of the Region-1 and the Region-2 current is located mostly in the afternoon sector and the dawn-side pair of the Region-1 and Region-2 current is skewed to the pre-dawn sector (Figure 3(b4)). The clockwise twist of the convection pattern reshapes the geospace plume. As shown in Figure 3(d4), the shape of the plasmasphere and the TEC contour follows the shape of the potential contour lines. The potential contours show a prominent dawn-dusk asymmetry. As positive storm effects occur primarily in the late afternoon to dusk (~14-19 MLT in Figure 3(c4)) at low and middle latitudes, the strong convection in the dusk sector transport plasma toward high latitudes. The plume structure follows the potential contours and the plume is biased to the dusk side. Another prominent feature during the main phase is the presence of TEC depletion channels. In the dusk sector, a low TEC channel expands from the equator and merges into the midlatitude (~45 MLAT) electron density/TEC trough region. There is another low-TEC channel located around 60 MLAT inside the auroral oval. Both TEC depletion channels (marked by red arrows in Figure 3(c4)) extend sunward. In the equatorial plane, the midlatitude depletion channel is located at the dusk edge of the plasmaspheric plume and we can see the plasmaspheric plume has become much narrower compared with its shape in the early main phase. We refer to this depletion of the TEC and the narrowing of the plasmaspheric plume as geospace plume “erosion”. We will discuss these two features in Sections 4.2.2.

In the last stage, 08:00~12:00UT, 03-31-2001, which is the storm recovery phase (Figure 3(a5)-(d5), the fifth column), the IMF turns northward and the ram pressure decreases. The ionospheric convection becomes much weaker (Figure 3(b5)). The two TEC depletion channels merge into one and cut across the tongue of ionization and leaves some polar cap patches (Figure 3(c5)). In the equatorial plane (Figure 3(d5)), the sunward driving of the plasmaspheric plume diminishes and the co-rotation takes over again. Due to the loss of the particles through the dayside to the open-field-line region, the size of the plasmasphere shrinks significantly with a plasmapause radius of 2 ~ 2.5R_E.

There are three prominent features from the simulation results. The first is that the equatorial plane mapping of the TEC colored contour resemble the shape of the plasmapause. Especially during the storm's main phase, their synchronized sunward expansion and the overlap of the two plumes is quite apparent. We will discuss the major cause of their linkage in Section 4.1. The second feature, as mentioned above, is the density depletion channels in the dusk sector at midlatitude. We investigate their role in eroding the dusk edge of the plasmasphere plume in Section 4.2. Thirdly, the ring current development with its dusk-preferred accumulation significantly impacts the distribution of the FACs and thus the electric fields, which eventually control to the geospace plume development. We investigate the relation between the ring current build-up and the geospace plume evolution in detail in Section 4.3.

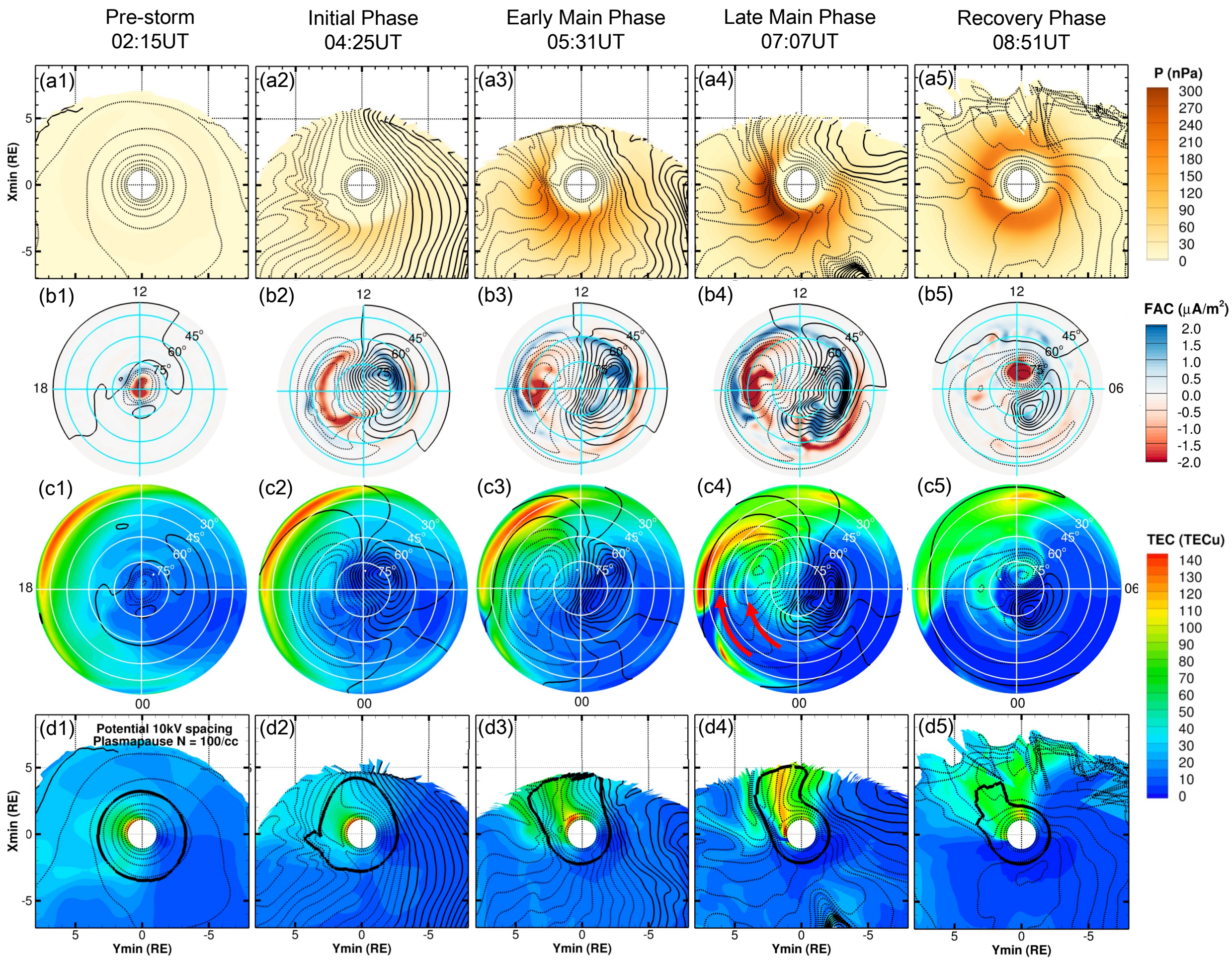

Figure 3. (a1)-(e1) to **(a5)-(e5)** show five stages of the storm (the 1^{st} period of southward IMF shaded in Figure 2) with each column, top to bottom, depicting the equatorial plane view of the ring current pressure, the ionospheric FAC, the ionospheric TEC and the equatorial plane mapping of the TEC and the plasmapause (heavy black contour). The thin black lines (dashed for negative values) are contours of the electric potential, with 10keV interval on equatorial plane (bottom row) and 20keV in the ionosphere (third row from top).

4. Discussion

4.1 Linkage between the plasmaspheric and the ionospheric plumes

Foster et al. (2002) first reported the overlap of the plasmaspheric plume with the magnetospheric mapping of the ionospheric plume during the March 31, 2001 storm. The IMAGE satellite and the World-wide TEC measurement jointly observed the resemblance of the two plumes for the second period of the southward IMF. Figure 4(a) shows the IMAGE EUV image of the plasmasphere at 21:23UT, March 31, 2001 (Source: http://euv.lpl.arizona.edu/euv/). Figure 4(b) is the World-wide TEC data (Source: Madrigal database) mapped to the equatorial plane using the magnetic field-line traced in the MAGE model. Figures 4(a) and (b) are adjusted to a similar length scale as Figure 4 of Moldwin et al., 2016. The plasmapause is located at approximately 2R_E on the nightside and the plasmaspheric drainage plume expands from the dusk edge of the plasmasphere toward the subsolar magnetopause (Figure 4(a)). The projection of the observed global TEC on the equatorial plane at 21:22UT (Figure 4(b)) shows similar shape and orientation with the plasmaspheric plume. Figure 4(c) gives the MAGE simulated plasmapause and TEC projected to the equatorial plane on the same color scale. The simulated plasmaspheric plume is co-located with the TEC plume which is consistent with the observations.

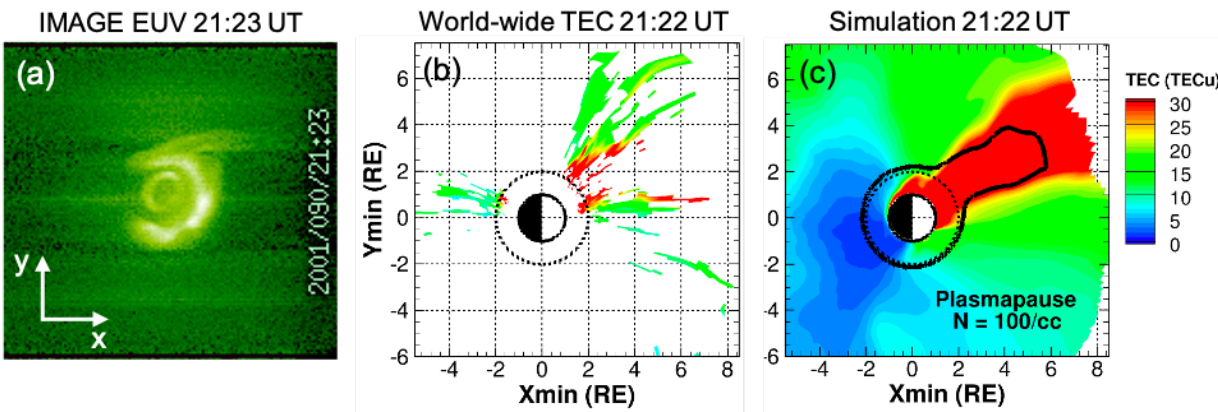

Figure 4. (a) IMAGE EUV image of the plasmasphere taken at 21:23UT, 03-31-2001. **(b)** The equatorial-plane projection of the global TEC measurement at 21:22UT, 03-31-2001, mapped by the MAGE magnetic field line. **(c)** The contour plot of the MAGE simulated plasmapause and TEC projection on the equatorial plane. The plasmasphere and the TEC are presented in SM coordinates. The sun is to the right. Black solid circle represents the Earth and the dashed black circle has a radius of 2R_E.

This overlap in the equatorial mapping of the two plumes can be seen throughout the storm. As described in Section 3 and shown in Figure 4, both the plasmasphere and the electron content co-rotate eastward when the two-cell potential pattern has not yet been established. During the strong southward IMF driving, e.g., at T = 650 ~ 950 min in Movie S1, the ionospheric two-cell convection dominates over the co-rotation. The evolution of the plumes is controlled by the dusk cell and follows the geometry of local electric potential contours. In the noon-to-dusk sector, the plumes extend from the low middle latitudes to the pole, which corresponds to the sunward expansion in the equatorial plane.

Compared to the SAMI3-RCM simulation of the same event (Huba & Sazykin, 2014), in our MAGE simulation, the plasmaspheric plume (from RCM) and the TEC (from TIEGCM) plume are driven by the midlatitude electric fields that are controlled by the same high-latitude electric field, but the mass exchange between the ionosphere and the plasmasphere is not included. However, the overlap and joint evolution of the two plumes are still successfully reproduced. This indicates that the electrodynamic coupling in the M-I-T system, rather than the mass connection, plays a dominant role in the formation and evolution of the geospace plume in both the plasmasphere and the ionosphere.

4.2 Westward ion drifts (WIDs) and their effect on the geospace plume

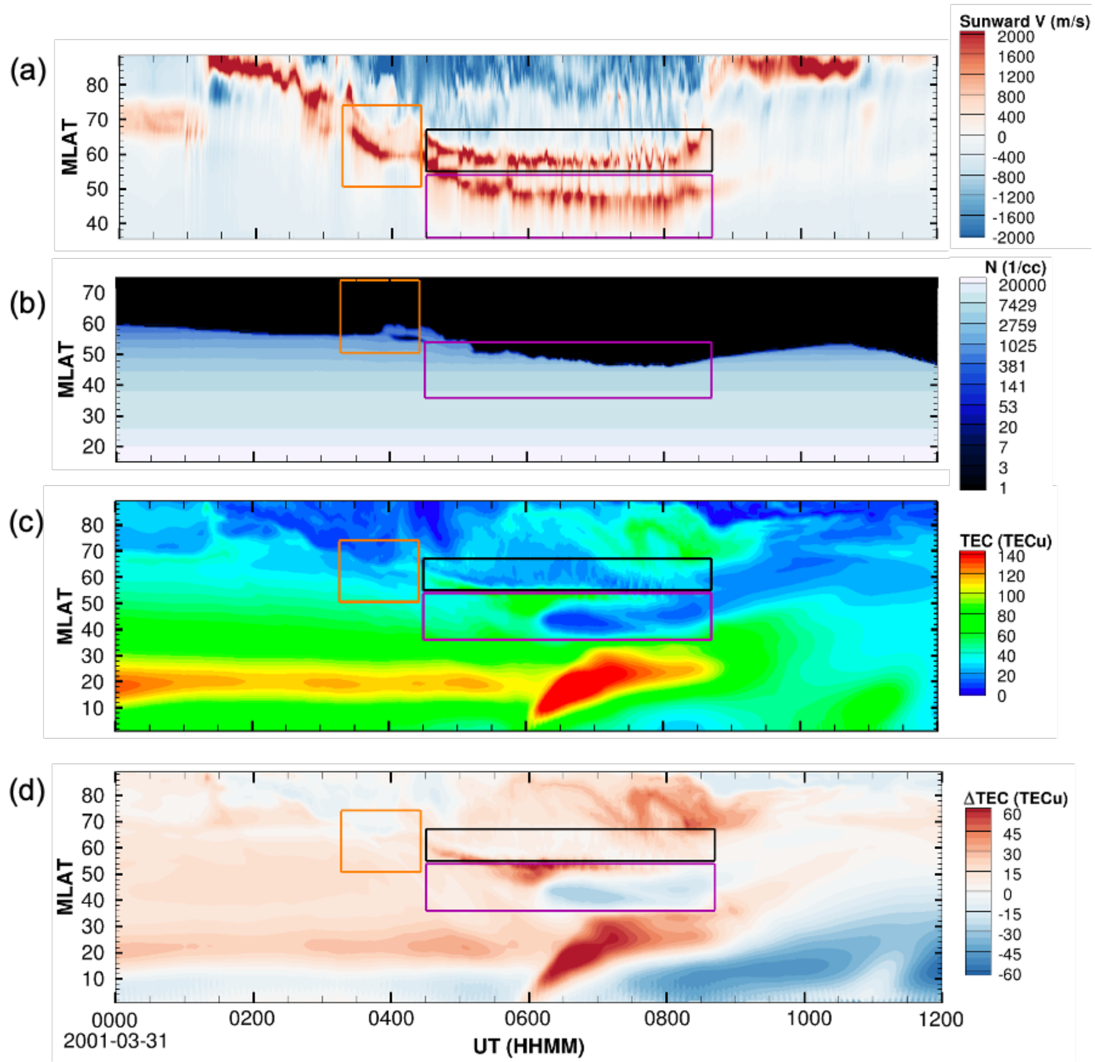

Figure 5. (a)-(d) Keograms of the simulated westward (sunward) ion drift velocity, plasmaspheric density, TEC and ΔTEC at 18 MLT. ΔTEC is calculated by subtracting the quiet-time (March 29, 2001) TEC from the storm-time TEC at the same UT. The colored boxes mark the sunward velocity peaks and the corresponding erosion region in the plasmaspheric density, TEC and ΔTEC. The boxes of the same color cover the same range of latitude in different panels. The orange box marks the WID in the initial phase; the purple box marks the WID velocity peak in the midlatitude; the black box marks the?????

To further investigate the geospace plume erosion on the dusk side, we sample the MAGE simulated ion drift velocity (from REMIX), ionospheric mapping of the plasmaspheric density (from RCM), TEC and ΔTEC (from TIEGCM) along 18 MLT for the first period of southward IMF (Figures 5(a) - (d)). The Y-axes of different panels cover different ranges of magnetic latitude since the variables are calculated in different MAGE component models. In Figure 5(a), the ion drift velocity is a combination of the corotation velocity and the **E**×**B** ion drift velocity in the SM coordinates. The red color signifies a westward (i.e., sunward at 18 MLT) direction, while the blue color signifies an eastward/tailward direction.

4.2.1 The plasmasphere finger

During the initial phase (around 01:30~04:30UT), when the two-cell convection pattern starts to establish, a single band of WID velocity peak moves from high latitude toward midlatitude (Figure 5(a)). A weak reduction in the TEC can be seen at the similar MLAT according to Figures 5(c) and (d). When the WID peak extends to 60 MLAT, it reaches the plasmapause and drives the expansion of a plasmasphere finger (Figure 5(b)), a f. The orange box in Figure 5(b) marks the period of finger development in the initial phase (T = 705~750 min in Movie S1) and Figure 6 shows a snapshot of the finger-like structure that develops at the dusk edge of the plasmapause and expands radially following the electric potential contour (marked by the orange arrows) at 04:24 UT. We can see from Figure 6 that the cause of the plasmaspheric finger is a result of the interaction between the plasmapause which is around 3.5 ~ 4R_E at the early stage of the storm and the equatorward-expanding dusk convection cell of the electric field.

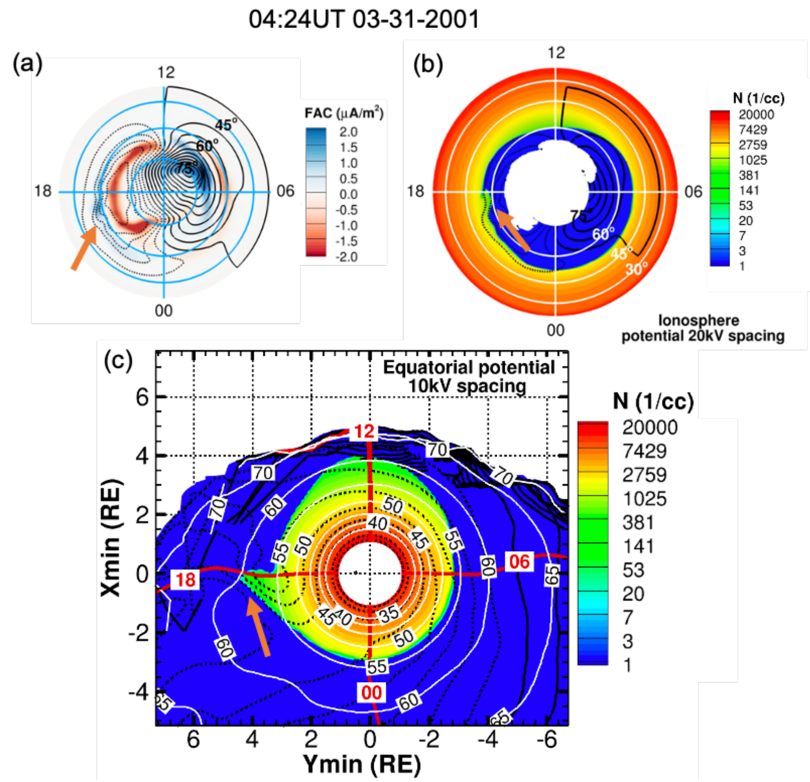

Figure 6. (a)-(c) Snapshots taken at 04:24UT 03-31-2001 at the end of the initial phase. **(a)** Simulated FAC in SM coordinates. **(b)** and **(c)** are ionospheric mapping and equatorial plane view of the plasmaspheric density with contour lines of the indicated MLT (red) and latitude (white) mapped to the plane. Black contour lines in **(a-b)** and **(c)** show electric potential with 20kV and 10kV intervals respectively, dashed for negative values. The orange arrows point to the location of the enhanced electric fields and the plasmasphere finger between 55 to 60 MLAT during the initial phase, which correspond to the westward drift velocity peak marked in Figure 5(a) by the box of the same color.

4.2.2 Erosion on the geospace plume

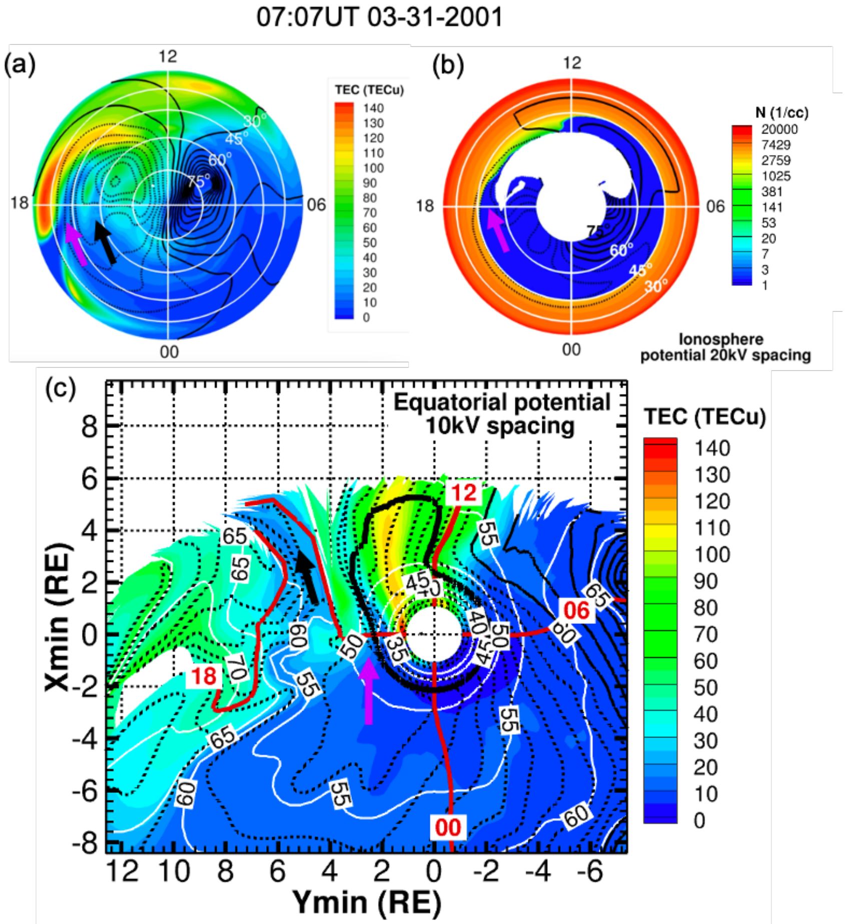

Figure 7. (a)-(c) Snapshots taken at 07:07UT 03-31-2001 in the late main phase. **(a)** Simulated TEC in SM coordinate. **(b)** and **(c),** same variables as in Figure 6. The purple and black arrows point to the locations of the density depletion, which correspond to the SAPS channel and the CRF marked in Figure 5 by the box of the same colors.

During the main phase (around 04:30~8:10UT, T = 750~970 min in Movie S1), the two-cell convection pattern has established, double-band WID velocity peaks appear (Figure 5(a)), with one peak located at higher latitudes around 60 MLAT marked by the black box and another located at midlatitudes around 45~50 MLAT marked by the purple box. As shown in Figure 5(b), the plasmapause in the purple box moves from 55 MLAT to 45 MLAT. The velocity peak around 60 MLT does not overlap with the plasmasphere and thus, cannot directly interact with and influence it. In Figure 5(c), two large WID velocity channels are collocated with regions of low TEC, which can be seen in both black and purple boxes. The TEC depletion effect along with the midlatitude subauroral velocity peak is much more prominent according to Figure 5(d), where the depletion in TEC and ionospheric electron densities is quite obvious. However, ΔTEC in the black box does not show a negative value, which means the decrease of the TEC around 60 MLAT may not be an obvious storm effect. Figure 7 shows the snapshots of TEC depletion and the plasmaspheric erosion corresponding to the double-band WID velocity channels (marked by the black and purple arrows). Figure 7(c) demonstrates clearly that in the equatorial plane, the midlatitude velocity peak (purple arrow) is collocated with TEC depletion and erodes the dusk edge of the plasmaspheric plume, while the higher latitude velocity peak (black arrow) is only coincident with a TEC depletion, since the plasmapause has been eroded to lower L-shell and latitude.

4.2.2.1 Erosion on the plasmasphere

The double-peak feature in the WIDs is examined by Lin et al. (2021), who used the MAGE model to perform a set of controlled numerical experiments and demonstrated that the diffuse electron precipitation plays a crucial role in causing the latitudinal structure of the SAPS electric field. Figures 8(a) - (d) show the sampled FAC, electron precipitation, ionospheric conductance and electric field strength along 18 MLT at 07:07UT 03-31-2001. The green shade marks the auroral region which consists of the diffuse electron precipitation and the mono-energetic electron precipitation. The electron precipitation increases the local ionization rate in the ionosphere E-region and enhances the Pedersen and Hall conductance. A portion of the Region-2 current is located equatorward of the diffuse electron precipitation, where the conductance is comparatively low. This leads to a strong poleward electrostatic field in the sub-auroral region marked by the orange shade. The sub-auroral polarization stream (SAPS) is the WID that is constrained between the low latitude boundary of the dusk-side diffuse electron precipitation and the low latitude boundary of the dusk-side Region-2 current. The SAPS velocity peaks around 45°~50° and it overlaps with the plasmapause, causing a sunward ion flow shown in Figure 8(f). The advection flow transports the cold plasma away from the plasmasphere and to the dayside, which explains the erosion on the plasmapause marked by the purple box in Figure 5(b). The velocity peak located at higher latitudes around 57° is inside the range of the Region-1 current. It peaks in the region between the diffuse and the mono-energetic precipitation where the conductance is also comparatively low and the closure of Region-1 and the Region-2 currents results in a strong electric field. This electric field causes WID velocity peak and we call it the convection return flow (CRF). The CRF does not interact with the plasmasphere, which is consistent with Figure 5(b).

4.2.2.1 Depletion of the TEC

Figure 8(g) shows the MLAT profile of TEC, where there are two electron density/TEC troughs with one co-located with the peak of CRF around 55 MLAT and the other located around 42 MLAT, to the equatorward of the SAPS peak. The factors that contribute to the depletion of the ionospheric TEC are much more complicated than the plasmaspheric erosion. The formation of the electron density trough is discussed by Lu et al. (2020), where they examined the rate of change for O^+ density in the TIEGCM, which is considered as a proxy for the electron content. In general, the rate of change is determined by the O^+ production and loss rate, ambipolar diffusion, neutral wind transport, and the $\mathbf{E}\times\mathbf{B}$ transport. Lu et al. gave a detailed analysis of the contribution from each process. They showed that the $\mathbf{E}\times\mathbf{B}$ transport is the major contributor to the formation of the sub-auroral electron density trough. This transport brings the low electron density into the high-density region, and this depletion is further enhanced with the increased loss/recombination rate of the ions at a higher temperature caused by the significantly enhanced frictional heating due to the strong ion drifts in the WID channel (Schunk et al., 1976). The analysis above is consistent with our results. However, the equatorward shift of the midlatitude electron density trough in Figure 8(g) indicates other transport effects and needs further investigation in the future.

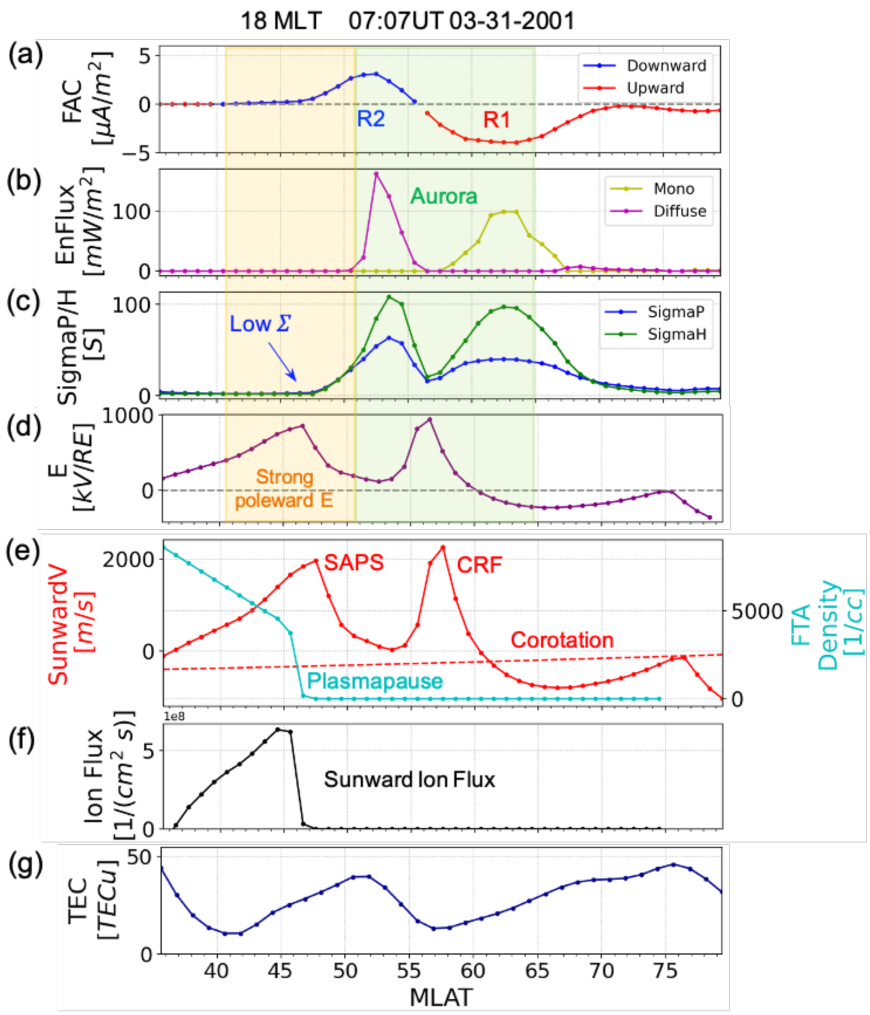

Figure 8. (a)-(e) Latitudinal profiles of REMIX ionospheric quantities sampled at 18 MLT and 07:07UT. **(a)** Upward Region-1(red) and downward Region-2 current (blue). **(b)** Energy flux of diffuse (magenta) and mono-energetic (olive) electron precipitation. **(c)** Pedersen conductance (blue) and Hall conductance (green). **(d)** Electric field strength. **(e)** Calculated E×B ion drift velocity (red) with corotation velocity shown by the dashed line. The cyan curve is the flux-tube-averaged (FTA) plasmaspheric density mapped to the ionospheric grid. **(f)** Calculated sunward ion flux based on density and ion drift velocity in **(e). (g)** Total electron content.

4.2.2.1 Data-model comparison on the erosion effect

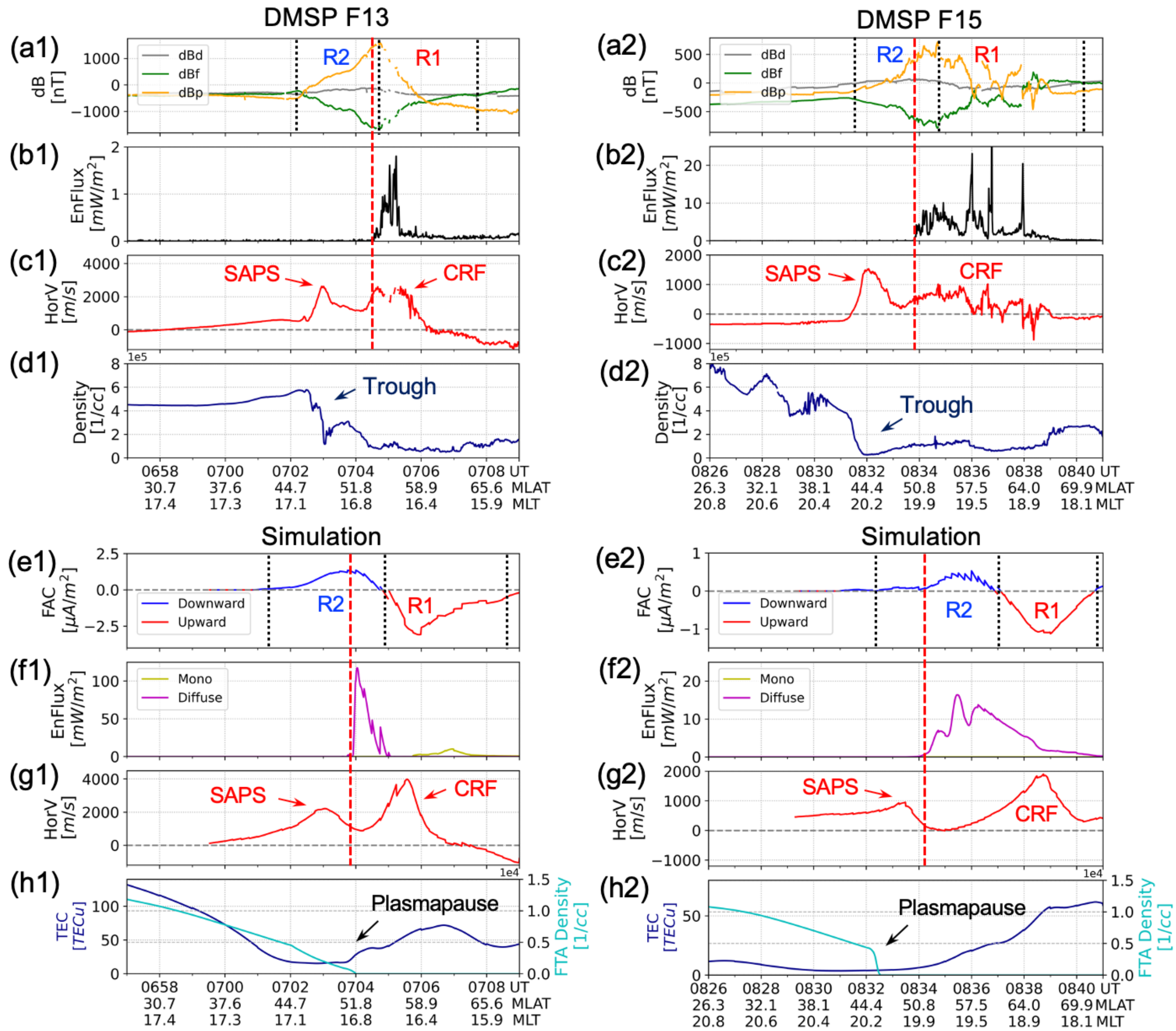

Figure 9. DMSP F13 and F15 (~850km in altitude) measurements at 06:57 ~ 07:09UT, March 31, 2001: **(a1)-(a2)** magnetic perturbation in the downward (dBd), forward (dBf) and perpendicular (horizontal cross-track) (dBp) direction relative to the satellite track direction; **(b1)-(b2)** precipitating electron energy flux; **(c1)-(c2)** horizontal cross-track sunward ion drift velocity; and **(d1)-(d2)** electron density. The dashed black lines in **(a1)-(a2)** divide the range of the Region-1 and the Region-2 currents based on the slopes of the magnetic perturbation curves. The dashed red line is the equatorward auroral boundary. Simulated quantities sampled along the satellite track: **(e1)-(e2)** field-aligned current; **(f1)-(f2)** energy flux of diffuse electron precipitation (magenta) and mono-energetic precipitation (olive); **(g1)-(g2)** simulated ion drift velocity in the DMSP horizontal cross-track sunward direction; **(h1)-(h2)** simulated electron density (navy) and flux-tube-averaged plasmaspheric density (black).

Sections 4.2.2.1 and 4.2.2.2 discuss the double-peak feature in WIDs on the dusk side and their effect on the plasmaspheric erosion and ionospheric TEC depletion. In this section, we investigate this subject with DMSP observations. Figure 9 shows a data-model comparison of the FAC, the ionospheric differential number flux of the electron precipitation, the horizontal ion drift velocity, and the electron density. Figures 9(a1) - (d1) and (a2) - (d2) are DMSP F13 and F15 measurements during 06:57 ~ 07:09UT and 08:26 ~ 08:41UT, 03-31-2001 respectively. Ranges of the Region-1 and the Region-2 currents can be derived from the magnetic field perturbation following the method from J. Liu et al. (2022), which are divided by the back dashed line in Figures 9(a1) and (a2). Figures 9(e1) - (h1) and (e2) - (h2) are the corresponding physical quantities from the MAGE simulation along the satellite trajectories. Since the satellites usually fly beyond the altitude range of TIEGCM, we plot the TEC and the plasmaspheric flux-tube-averaged (FTA) density instead. The dashed red line is the equatorward auroral boundary using the same criteria as in Figure 8.

Figures 9(a1) - (d1) and (a2) - (d2) show that dusk-side electron precipitation is located mostly within the range of the Region-1 current with a slight overlap on the Region-2 current. The SAPS is located in the sub-auroral region within the range of the Region-2 current. The CRF covers the region between the Region-1 and Region-2 current and some portion of the Region-1 current. The spikes in the electron precipitation, e.g., around 55 MLAT at 07:05UT correspond to the dips in the CRF velocity. The large velocity of SAPS (Figure 9(c1)) is collocated with an acute trough in the ionospheric electron density. The electron density is also low at higher latitudes, corresponding to the location of CRF. This is consistent with the result shown in Figure 8.

Compared with the DMSP data, the simulation predicts similar location of the Region-1/2 currents and electron precipitation. The model overestimates the strength of the precipitation energy flux in Figure 9(f1), but according to the following REMIX output it is transient and it does not impact the ionospheric conductance much. In terms of the WID velocity, the double-band feature of WIDs, SAPS and CRF peaks, are successfully reproduced. The SAPS velocity is around 2000 m/s at 07:03UT and 1000m/s at 08:33UT, which are in reasonable agreement with the observations.

In Figures 9(h1) and (h2), the location of the plasmapause and the TEC depletion can be seen and compared with the observations. The simulated TEC troughs corresponding to SAPS are much broader than the electron density troughs in the observation. The FTA plasmaspheric density, on the other hand, has good agreement with the observations of the electron density in Figures 9(d1) and (d2): At 07:03UT (near 48 MLAT,17 MLT), in the observation (Figure 9(d1)), the SAPS velocity peak still overlaps with the region with substantial electron content and causing a density trough to mirror the SAPS peak. In the simulation (Figure 9(h1)), the SAPS peak also overlaps with a portion of the plasmasphere which causes sunward plasmaspheric particle transport. In the later satellite pass at 08:32UT (near 46 MLAT, 20 MLT) as shown in Figure 9(d2), the SAPS velocity peak corresponds to a substantially depleted electron density that forms a distinct boundary in the density profile. In the simulation (Figure 9(h2)), the same sharp drop in the FTA density is captured by the model. Combined with the analysis of the sunward ion flux caused by SAPS at the plasmapause in Figure 8(e)-(f), this data-model comparison confirms the effect of SAPS in depleting the local plasma content.

In Section 4.2, we have discussed the formation of the WIDs and investigated their role in depleting the local plasma density. During storm main phase, in both simulation and observation, two velocity peaks can be found in the WIDs. The one at the midlatitude is the SAPS channel. The transportation effect of SAPS causes the erosion of the plasmapause at its dusk side and the TEC depletion in the trough region. In the next section, we further investigate the factors that determine the spatial distribution of Region-2 current and the electron precipitation that lead to the SAPS electric field and their relation to the geospace plume evolution.

4.3 Relationship between ring current build-up and geospace plume development

As discussed in Section 4.2, the Region-2 current and electron precipitation directly control the SAPS electric field development in the ionosphere. In this section, we further explore the major factors in the magnetosphere that drive SAPS development and the geospace plume evolution from the perspective of M-I coupling.

Figures 10(a) and Figure11(a) show contours of the specified values in the plasma profile as a marker of the plasmapause (black), the ring current ion pressure (red), the electron pressure (green), the equatorial mapping of the energy flux of diffuse electron precipitation (orange), the FAC (background) and the electrostatic potential (light solid and dashed contours) at the beginning (04:48UT) and the end (07:41UT) of the storm main phase. The variable values enclosed by the colored contour lines are larger than the contour values. The contour values are chosen to best describe the spatial distribution of the variables (see Figure S1). The red arrows point to the critical region, where the dusk-side Region-2 current (in blue) is located. At the sunward azimuthal edge of the ring current ion pressure (represented by the magenta contour), the large pressure gradient distorts the magnetic field lines and generates the Region-2 current that connects to the partial ring current and flows into the ionosphere. The magnetospheric source region of diffuse precipitation is located in the region with high electron pressure and it partially overlaps with the Region-2 current. This results in a strong SAPS electric field co-located with the low-latitude portion of the Region-2 current where there is little electron precipitation. This result is consistent with previous MAGE modeling work of SAPS (Lin et al., 2021) and earlier works describing the basic physics of SAPS (e.g., Foster & Vo, 2002).

During the period of geospace plume erosion by SAPS (from Figure 11(a) to Figure 11(a)), the high electron pressure region, which is the source region of the electron precipitation, is always located at the outer boundary of the ring current ion pressure 100 nPa contour. As a result, the electron precipitation always covers a portion of the Region-2 current which maintains the persistent SAPS electric field located at the inner boundary of the ring current contour and the dusk edge of the plasmapause. The strong SAPS electric field dominates the spatial distribution of the electric potential and evolves the plasmaspheric plume into the dusk side. The joint evolution of the ring current and the plasmasphere is shown in Movie S3 and a similar spatial relation of the two is observed by the IMAGE satellite (Figure S2).

We now ask, what determines the spatial distributions of the ring current electron and ion pressure that impact the source regions of diffuse electron precipitation and the Region-2 currents? The cold plasmaspheric protons are subject to the **E**×**B** drift and corotation. Besides these two drifts, the hot protons and electrons, after being transported to the inner magnetosphere, are also subjected to gradient/curvature drift in opposite directions. In RCM, the total drift effect is represented by the effective potential defined by adding the term $V^{-2/3} \cdot \lambda_{i,k}/e$ to the equatorial electric potential (Toffoletto et al., 2003). This effective electric potential for species *i* at energy channel *k* is given by

$$\phi_{eff,k,i} = \phi_I + \lambda_{i,k} \cdot V^{-\frac{2}{3}}/e + \phi_c \tag{3}$$

where $\lambda_{i,k}$ is the energy invariant for species *i* at channel *k* in RCM and the closed magnetic flux tube volume *V* is given by

$$V = \int \frac{ds}{B_{MHD}} \tag{4}$$

Figures 10, 11(b) - (d) show the flux tube content (η) in the magnetic flux tube from the RCM characteristic energy channels of the plasmasphere ($\lambda_0 = 0$), hot protons and hot electrons at the beginning and the end of the storm main phase. The proton and the electron channels shown (λ_p= 1639.46, λ_e =-234.21, in RCM units, $eV \cdot (R_E/nT)^{\frac{2}{3}}$) are the ones that contribute most to the total proton pressure and the total electron pressure (as well as the diffuse precipitation energy flux) respectively. The corresponding energy of the proton and the electron at the selected channels is around 80 keV and 8 keV at the location of the ring current and the electron precipitation. The effective potential of the channel is plotted as black contour lines with dashed lines for negative values.

Comparing the effective electric potential contours in Figures 10 (b) - (d), we can see the gradient and curvature term in the proton effective electric field ($Potential\_P$) dominates the inner magnetosphere and is a result of the comparatively large energy invariant of that proton channel. The electron effective electric potential ($Potential\_E$) contours look similar to the plasmaspheric electric potential ($Potential\_0$)) especially outside the geosynchronous orbit, since the gradient and curvature term for electrons is comparatively weak due to their lower particle energy. During the early main phase, the ring current particles have just been transported by the convection electric field to the inner magnetosphere and started to drift following their effective electric potential contours. Meanwhile, the plasmaspheric plume expands sunward driven by the convection electric field. At this moment, the η distributions of the plasmasphere, proton and electron are approximately symmetric about the x-axis (Y = 0) and the conditions for the SAPS formation have just started to appear on the dusk edge of the plasmasphere.

At the late main phase, as shown in Figure 11(c), the η distribution shows that the ring current hot protons have drifted westward from the nightside and penetrated deep inside $2R_E$ on the dayside (marked by the yellow arrow). The Region-2 current originating at the outer edge of the partial ring current beyond $2R_E$ has shifted toward the dayside accordingly (in Figure 11(a)). The SAPS electric field have been very strong and dominated the geometry of Potential_0 and Potential_E. On one hand, it causes the plamaspheric plume to move to the dusk side. On the other hand, the hot electrons (in Figure 11(d)) are obstructed by the strong dusk-side electric fields with major contribution from SAPS. The electrons accumulate outside the SAPS flow channel around $3R_E$ and form a sharp edge in the electron η distribution (marked by the orange arrow). This leads to a distinct equatorward edge of the ionospheric diffuse precipitation and the absence of electron precipitation in part of the Region-2 current that helps to maintain the strong SAPS electric field.

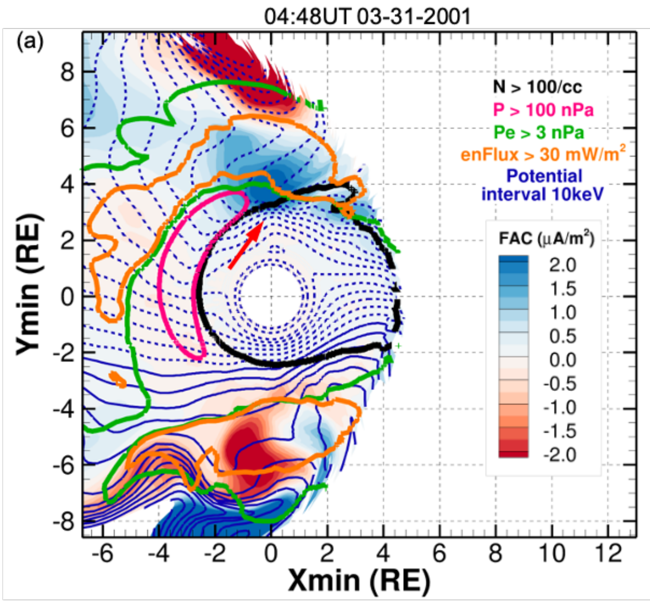

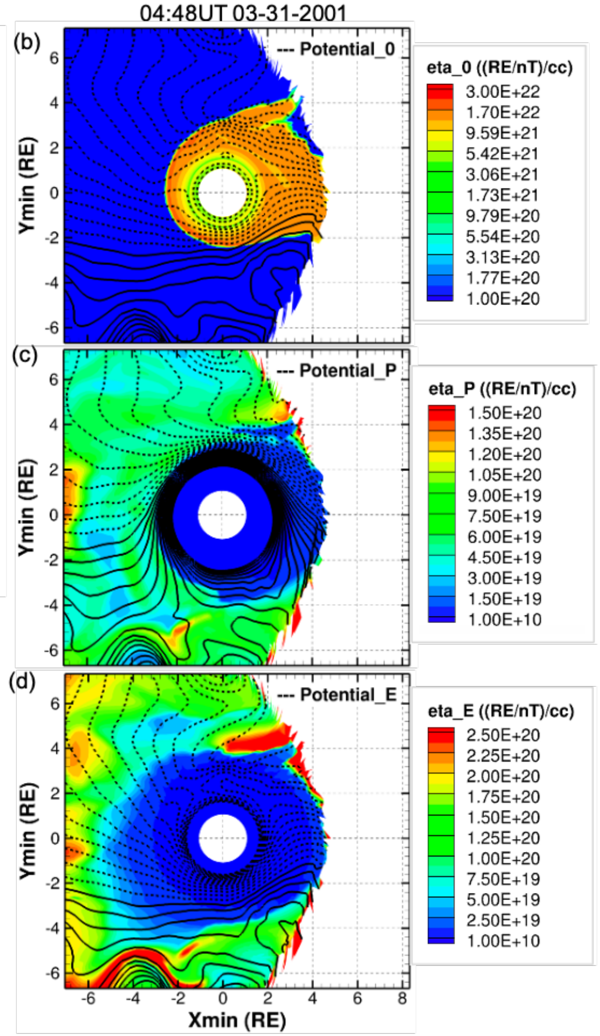

Figure 10. (a) Contour plots of the equatorial plane view of plasmapause (black), ring current pressure (pink), electron pressure (green), equatorial energy flux of diffuse electron precipitation (orange), electrostatic potential with 10kV spacing (navy, dashed for negative values) and FAC (red-blue) on the equatorial plane at the early main phase. The red arrow points to the location where the Region-2 current is strong while the diffuse precipitation is weak and the resultant (SAPS) electrostatic field is intense. **(b)-(d)** Contour plots of the RCM η variable for the plasmaspheric energy channel, the proton energy channel that contributes most to the ring current pressure and the electron energy channel that contributes most to the electron pressure/diffuse precipitation energy flux and their corresponding effective electric potential on the equatorial plane.

The analysis above demonstrates that the storm-time energy-dependent electron and proton drifts determine the spatial distribution of Region-2 currents and diffuse electron precipitation. The ring current ion can overcome the existing SAPS electric field and penetrate into deeper L-shell at dayside, while the ring current electrons cannot due to their featured adiabatic invariants of their drifts. This delicate balance between the energy-dependent gradient/curvature drift and the **E**×**B** drifts self-consistently maintains the SAPS electric field to further erode the dusk-side plasmasphere and push the plasmaspheric plume shifting toward the dusk side.

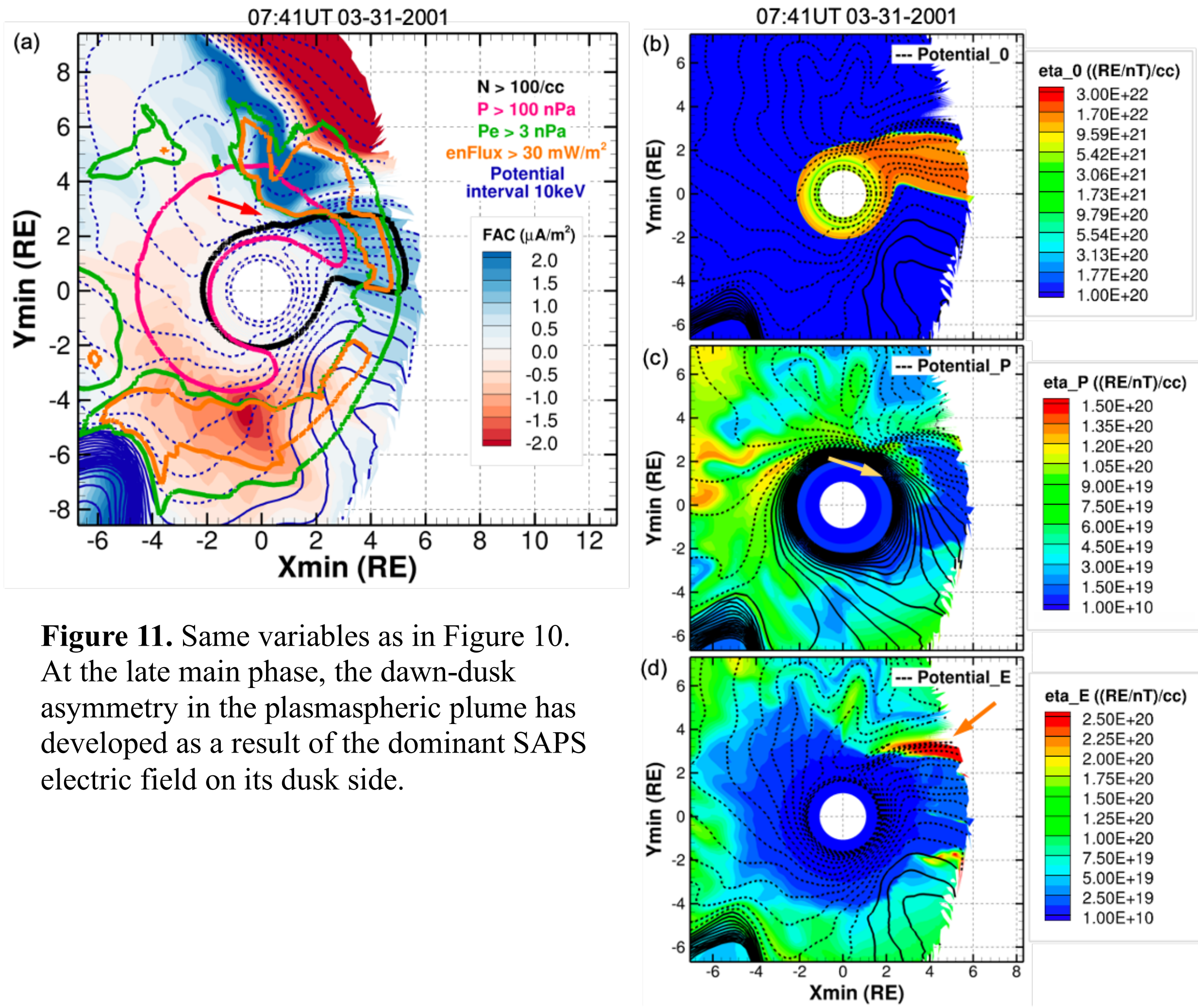

Figure 11. Same variables as in Figure 10. At the late main phase, the dawn-dusk asymmetry in the plasmaspheric plume has developed as a result of the dominant SAPS electric field on its dusk side.

4.5 Model limitations

The MAGE simulation of the March 31, 2001 storm presented above demonstrates clearly the close relation between the global-scale convection, ring current build-up, FAC, and electron precipitation which dynamically alter the geospace plume system. However, there are some limitations. First, the model did not include the plasma transport between the plasmasphere and the ionosphere. Although, as discussed in Section 1.2.2.2, plasmaspheric refilling is much slower compared with the dynamic transport of the plasma within the plasmasphere and ionosphere during the storm main phase (Lawrence et al., 1999; Denton et al., 2012; Krall et al., 2014), plasma exchange between the plasmasphere and ionosphere can be important in the storm recovery phase (Carpenter & Lemaire, 1997). Second, as discussed in Section 4.3, during the later stage of the storm main phase, the simulated ring current overlaps with the plasmasphere, especially in the plume region. In this work, our model did not include ring current ion loss due to the EMIC wave scattering (Erlandson & Ukhorskiy, 2001; Goldstein et al., 2003), although it is possible that ion precipitation may affect the ionospheric conductance and feed back to the magnetospheric system (Tian et al., 2022). Furthermore, inside the plasmasphere, the energetic electrons resonate with hiss waves and contribute to diffuse electron precipitation (Ma et al., 2021). The current version of the model did not take into account such wave-particle interactions. We are working on including these important precipitation mechanisms to better inform the ring current particle loss and ionospheric precipitation in future versions of the model (Bao et al., 2022; Lin et al., 2022).

4 Summary and Conclusions

In this paper, we investigate the evolution of the geospace plume during the March 31, 2001 superstorm using the MAGE model, which coupled the global and inner magnetosphere, the ionosphere and the thermosphere. Combined with satellite observations, we used the MAGE simulation to address the three major science questions raised in the introduction section.

The first question is the cause of the linkage and joint evolution of the two counterparts of the geospace plume, the plasmaspheric plume and the ionospheric SED plume. We conclude that the **E**×**B** transport of the plasma by the coupled magnetosphere-ionosphere electric field is the major process that causes the plasmaspheric plume and the ionospheric SED plume to evolve in a similar way and to have co-located footprints on the equatorial plane.

The second and third science questions are closely tied together. The second science question focuses on identifying the specific processes that are important for shaping the plasmasphere and the ionosphere plume. The third science question explores the relationship between the build-up of the ring current and the development of the geospace plume. The simulation shows that geospace plume in the equatorial plane expands sunward due to the convection electric field in the early main phase. The plume shifts toward the dusk side in the late main phase. We also find two channels of TEC depletion, with one in the ionosphere midlatitude trough region, corresponding to the dusk edge of the plasmasphere, and the other at higher latitudes inside the auroral oval. By investigating the related physical quantities along 18 MLT and comparing with DMSP observations, we find that the westward SAPS flow is the major cause of the erosion on the dusk edge of the plasmasphere and duskward shift of the geospace plume, which answers science question two. We further investigate the cause of the spatial distributions of the Region-2 currents and diffuse precipitation that are responsible for the occurrence of SAPS by analyzing the effective electric fields of ring current protons and electrons. Region-2 current is located at the sunward boundary of the ring current mostly contributed by hot protons, where the pressure gradient distorts the magnetic field. Due to the energy-dependent charged particle drifts, the ring current pressure is located preferentially on the dusk side. The region of energetic ring current electrons, as the source region of the diffuse precipitation, are at larger L-shells compared to the region of high ion pressure. As a result, the SAPS electric field is generated at the location where a part of the Region-2 current does not overlap with the diffuse precipitation and the ionospheric conductance is low. The analysis of the RCM energy channels shows the ring current ions can overcome the existing SAPS electric field and penetrate into deeper L-shell at dayside, while the ring current electrons cannot due to their featured adiabatic invariants of their drifts. This delicate balance between the energy-dependent gradient/curvature drift and the **E**×**B** drifts self-consistently maintains the SAPS electric field. We conclude that the intrinsic cause of the SAPS and the resulting plasmasphere erosion as well as the plume geometry is the energy-dependent drifts of the ring current electrons and ions that impact the coupled geospace system.

Acknowledgments

This work is supported by NASA DRIVE Science Center for Geospace Storms (CGS) grant 80NSSC22M0163, NASA O2R grant 80NSSC19K0241, NASA GCR grant 80NSSC17K0013 and LWS grant 80NSSC20K0356. Dr. Viacheslav Merkin gratefully acknowledges support from NASA LWS grants 80NSSC19K0080 and 80NSSC19K0071. We would like to acknowledge the use of computational resources (doi:10.5065/D6RX99HX) at the NCAR-Wyoming Supercomputing Center provided by the National Science Foundation and the State of Wyoming, and supported by NCAR's Computational and Information Systems Laboratory. Dr. Shanshan Bao thanks Dr. Joe Huba and Dr. Roger Varney for the valuable discussion on the modeling work. The OMNI data are obtained from https://cdaweb.gsfc.nasa.gov/index.html/; the World-wide TEC data and the DMSP data are provided by the CEDAR Madrigal Database (http://cedar.openmadrigal.org/index.html); the simulation data selected for figures in this paper are stored and published on Zenodo (via: https://zenodo.org/record/7843840).

References

Bao, S. (2019). Large-scale Coupled Models of the Inner Magnetosphere. Diss., Rice University. Retrieved from https://hdl.handle.net/1911/107801.

Bao, S., Toffoletto, F., Yang, J., Sazykin, S., & Wiltberger, M. (2021). Coupling the Rice Convection Model-Equilibrium to the Lyon-Fedder-Mobarry Global Magnetohydrodynamic Model. *Journal of Geophysical Research: Space Physics*, *126*(8). https://doi.org/10.1029/2020JA028973

Bao, S., Lin, D., Sorathia, K., Wang, D., Toffoletto, F., Merkin, V., et al. (2022). Wave-dependent ring current electron loss and magnetospheric precipitation during a geospace storm. *AGU Fall Meeting Abstracts*, *2022*, SM22F-1988.

Burch, J. L., Mitchell, D. G., Sandel, B. R., Brandt, P. C., & Wüest, M. (2001). Global dynamics of the plasmasphere and ring current during magnetic storms. *Geophysical Research Letters*, *28*(6), 1159–1162. https://doi.org/10.1029/2000GL012413

Carpenter, D. L., & Lemaire, J. (1997). Erosion and recovery of the plasmasphere in the plasmapause region. *Space Science Reviews*, *80*(1/2), 153–179. https://doi.org/10.1023/A:1004981919827

Cramer, W. D., Raeder, J., Toffoletto, F. R., Gilson, M., & Hu, B. (2017). Plasma sheet injections into the inner magnetosphere: Two-way coupled OpenGGCM-RCM model results. *Journal of Geophysical Research: Space Physics*, *122*(5), 5077–5091. https://doi.org/10.1002/2017JA024104

De Zeeuw, D. L., Sazykin, S., Wolf, R., Gombosi, T., Ridley, A., & Toth. (2004). Coupling of a global MHD code and an inner magnetospheric model: Initial results. *Journal of Geophysical Research*, *109*(A12), A12219. https://doi.org/10.1029/2003JA010366

Denton, R. E., Wang, Y., Webb, P. A., Tengdin, P. M., Goldstein, J., Redfern, J. A., & Reinisch, B. W. (2012). Magnetospheric electron density long-term (>1 day) refilling rates inferred from passive radio emissions measured by IMAGE RPI during geomagnetically quiet times: MAGNETOSPHERIC ELECTRON DENSITY REFILLING RATES. *Journal of Geophysical Research: Space Physics*, *117*(A3), n/a-n/a. https://doi.org/10.1029/2011JA017274

Erlandson, R. E., & Ukhorskiy, A. J. (2001). Observations of electromagnetic ion cyclotron waves during geomagnetic storms: Wave occurrence and pitch angle scattering. *Journal of Geophysical Research: Space Physics*, *106*(A3), 3883–3895. https://doi.org/10.1029/2000JA000083

Fagundes, P. R., Cardoso, F. A., Fejer, B. G., Venkatesh, K., Ribeiro, B. A. G., & Pillat, V. G. (2016). Positive and negative GPS-TEC ionospheric storm effects during the extreme space weather event of March 2015 over the Brazilian sector: POSITIVE AND

NEGATIVE IONOSPHERIC STORM. *Journal of Geophysical Research: Space Physics*, *121*(6), 5613–5625. https://doi.org/10.1002/2015JA022214

Foster, J. C., & Burke, W. J. (2002). SAPS: A new categorization for sub-auroral electric fields. *Eos, Transactions American Geophysical Union*, *83*(36), 393. https://doi.org/10.1029/2002EO000289

Foster, J. C., & Vo, H. B. (2002). Average characteristics and activity dependence of the subauroral polarization stream: SUBAURORAL POLARIZATION STREAM. *Journal of Geophysical Research: Space Physics*, *107*(A12), SIA 16-1-SIA 16-10. https://doi.org/10.1029/2002JA009409

Foster, J. C., Erickson, P. J., Coster, A. J., Goldstein, J., & Rich, F. J. (2002). Ionospheric signatures of plasmaspheric tails. *Geophysical Research Letters*, *29*(13), 1623. https://doi.org/10.1029/2002GL015067

Foster, J. C., Erickson, P. J., Coster, A. J., Thaller, S., Tao, J., Wygant, J. R., & Bonnell, J. W. (2014). Storm time observations of plasmasphere erosion flux in the magnetosphere and ionosphere: Foster et al.: Plasmasphere Erosion Flux. *Geophysical Research Letters*, *41*(3), 762–768. https://doi.org/10.1002/2013GL059124

Foster, J. C., Erickson, P. J., Walsh, B. M., Wygant, J. R., Coster, A. J., & Zhang, Q. (2020). Multi-Point Observations of the Geospace Plume. In Q. Zong, P. Escoubet, D. Sibeck, G. Le, & H. Zhang (Eds.), *Geophysical Monograph Series* (1st ed., pp. 243–264). Wiley. https://doi.org/10.1002/9781119509592.ch14

Foster, J.C., Rideout, W., Sandel, B., Forrester, W. T., & Rich, F. J. (2007). On the relationship of SAPS to storm-enhanced density. *Journal of Atmospheric and Solar-Terrestrial Physics*, *69*(3), 303–313. https://doi.org/10.1016/j.jastp.2006.07.021

Foster, John C. (1993). Storm time plasma transport at middle and high latitudes. *Journal of Geophysical Research: Space Physics*, *98*(A2), 1675–1689. https://doi.org/10.1029/92JA02032

Gallagher, D. L., Craven, P. D., & Comfort, R. H. (2000). Global core plasma model. *Journal of Geophysical Research: Space Physics*, *105*(A8), 18819–18833. https://doi.org/10.1029/1999JA000241

Goldstein, J. (2004). Simultaneous remote sensing and in situ observations of plasmaspheric drainage plumes. *Journal of Geophysical Research*, *109*(A3), A03202. https://doi.org/10.1029/2003JA010281

Goldstein, J. (2007). Plasmasphere Response: Tutorial and Review of Recent Imaging Results. *Space Science Reviews*, *124*(1–4), 203–216. https://doi.org/10.1007/s11214-006-9105-y

Goldstein, J., & Sandel, B. R. (2005). The global pattern of evolution of plasmaspheric drainage plumes. In J. Burch, M. Schulz, & H. Spence (Eds.), *Geophysical Monograph Series* (Vol. 159, pp. 1–22). Washington, D. C.: American Geophysical Union. https://doi.org/10.1029/159GM02

Goldstein, J., Sandel, B. R., Hairston, M. R., & Reiff, P. H. (2003). Control of plasmaspheric dynamics by both convection and sub-auroral polarization stream: PLASMASPHERIC DYNAMICS. *Geophysical Research Letters*, *30*(24). https://doi.org/10.1029/2003GL018390

Goldstein, J., Burch, J. L., & Sandel, B. R. (2005). Magnetospheric model of subauroral polarization stream: MAGNETOSPHERIC SAPS MODEL. *Journal of Geophysical Research: Space Physics*, *110*(A9). https://doi.org/10.1029/2005JA011135

Goldstein, J., Thomsen, M. F., & DeJong, A. (2014). In situ signatures of residual plasmaspheric plumes: Observations and simulation. *Journal of Geophysical Research: Space Physics*, *119*(6), 4706–4722. https://doi.org/10.1002/2014JA019953

Huba, J., & Krall, J. (2013). Modeling the plasmasphere with SAMI3: MODELING THE PLASMASPHERE WITH SAMI3. *Geophysical Research Letters*, *40*(1), 6–10. https://doi.org/10.1029/2012GL054300

Huba, J. D., & Sazykin, S. (2014). Storm time ionosphere and plasmasphere structuring: SAMI3-RCM simulation of the 31 March 2001 geomagnetic storm. *Geophysical Research Letters*, *41*(23), 8208–8214. https://doi.org/10.1002/2014GL062110

Huba, J. D., Sazykin, S., & Coster, A. (2017). SAMI3-RCM simulation of the 17 March 2015 geomagnetic storm. *Journal of Geophysical Research: Space Physics*, *122*(1), 1246–1257. https://doi.org/10.1002/2016JA023341

Krall, J., Huba, J. D., Denton, R. E., Crowley, G., & Wu, T.-W. (2014). The effect of the thermosphere on quiet time plasmasphere morphology. *Journal of Geophysical Research: Space Physics*, *119*(6), 5032–5048. https://doi.org/10.1002/2014JA019850

Lawrence, D. J., Thomsen, M. F., Borovsky, J. E., & McComas, D. J. (1999). Measurements of early and late time plasmasphere refilling as observed from geosynchronous orbit. *Journal of Geophysical Research: Space Physics*, *104*(A7), 14691–14704. https://doi.org/10.1029/1998JA900087

Lemaire, J. F., Gringauz, K. I., Carpenter, D. L., & Bassolo, V. (1998). *The Earth's Plasmasphere* (1st ed.). Cambridge University Press. https://doi.org/10.1017/CBO9780511600098

Lin, C. H., Richmond, A. D., Heelis, R. A., Bailey, G. J., Lu, G., Liu, J. Y., et al. (2005). Theoretical study of the low- and midlatitude ionospheric electron density enhancement during the October 2003 superstorm: Relative importance of the neutral wind and the electric field. *Journal of Geophysical Research*, *110*(A12), A12312. https://doi.org/10.1029/2005JA011304

Lin, D., Wang, W., Scales, W. A., Pham, K., Liu, J., Zhang, B., et al. (2019). SAPS in the 17 March 2013 Storm Event: Initial Results From the Coupled Magnetosphere-Ionosphere-Thermosphere Model. *Journal of Geophysical Research: Space Physics*, *124*(7), 6212–6225. https://doi.org/10.1029/2019JA026698

Lin, D., Sorathia, K., Wang, W., Merkin, V., Bao, S., Pham, K., et al. (2021). The role of diffuse electron precipitation in the formation of subauroral polarization streams. *Journal of Geophysical Research: Space Physics*. https://doi.org/10.1029/2021JA029792

Lin, D., Wang, W., Merkin, V., Bao, S., Sorathia, K., Pham, K., et al. (2022). Characterizing auroral precipitation and ionospheric conductance with the Multiscale Atmosphere-Geospace Environment model. *AGU Fall Meeting Abstracts*, *2022*, SA24A-01.

Lin, D., Wang, W., Merkin, V. G., Huang, C., Oppenheim, M., Sorathia, K., et al. (2022). Origin of Dawnside Subauroral Polarization Streams During Major Geomagnetic Storms. *AGU Advances*, *3*(4). https://doi.org/10.1029/2022AV000708

Liu, J., Higuchi, T., Lyons, L. R., Ohtani, S., Wu, J., Zou, Y., et al. (2022). The Occurrence of Embedded Region 1 and 2 Currents Depends on Geomagnetic Activity Level. *Journal of Geophysical Research: Space Physics*, *127*(11). https://doi.org/10.1029/2022JA030539

Liu, Jing, Wang, W., Burns, A., Yue, X., Zhang, S., Zhang, Y., & Huang, C. (2016). Profiles of ionospheric storm-enhanced density during the 17 March 2015 great storm. *Journal of*

Geophysical Research: Space Physics, *121*(1), 727–744. https://doi.org/10.1002/2015JA021832

Lu, G., Zakharenkova, I., Cherniak, I., & Dang, T. (2020). Large-Scale Ionospheric Disturbances During the 17 March 2015 Storm: A Model-Data Comparative Study. *Journal of Geophysical Research: Space Physics*, *125*(5). https://doi.org/10.1029/2019JA027726

Ma, Q., Li, W., Zhang, X. -J., Bortnik, J., Shen, X. -C., Connor, H. K., et al. (2021). Global Survey of Electron Precipitation due to Hiss Waves in the Earth's Plasmasphere and Plumes. *Journal of Geophysical Research: Space Physics*, *126*(8). https://doi.org/10.1029/2021JA029644

Merkin, V. G., & Lyon, J. G. (2010). Effects of the low-latitude ionospheric boundary condition on the global magnetosphere: IONOSPHERE/MAGNETOSPHERE GLOBAL EFFECTS. *Journal of Geophysical Research: Space Physics*, *115*(A10), n/a-n/a. https://doi.org/10.1029/2010JA015461

Moldwin, M. B., Zou, S., & Heine, T. (2016). The story of plumes: the development of a new conceptual framework for understanding magnetosphere and ionosphere coupling. *Annales Geophysicae*, *34*(12), 1243–1253. https://doi.org/10.5194/angeo-34-1243-2016

Pembroke, A., Toffoletto, F., Sazykin, S., Wiltberger, M., Lyon, J., Merkin, V., & Schmitt, P. (2012). Initial results from a dynamic coupled magnetosphere-ionosphere-ring current model. *Journal of Geophysical Research: Space Physics*, *117*(A2), 2011JA016979. https://doi.org/10.1029/2011JA016979

Pham, K. H., Zhang, B., Sorathia, K., Dang, T., Wang, W., Merkin, V., et al. (2022). Thermospheric Density Perturbations Produced by Traveling Atmospheric Disturbances

During August 2005 Storm. *Journal of Geophysical Research: Space Physics*, *127*(2). https://doi.org/10.1029/2021JA030071

Pulkkinen, T. I., Tsyganenko, N. A., & Friedel, R. H. W. (Eds.). (2005). *The Inner Magnetosphere: Physics and Modeling* (Vol. 155). Washington, D. C.: American Geophysical Union. https://doi.org/10.1029/GM155

Qian, L., Burns, A. G., Emery, B. A., Foster, B., Lu, G., Maute, A., et al. (2014). The NCAR TIE-GCM: A Community Model of the Coupled Thermosphere/Ionosphere System. In Joseph Huba, R. Schunk, & G. Khazanov (Eds.), *Geophysical Monograph Series* (pp. 73–83). Chichester, UK: John Wiley & Sons, Ltd. https://doi.org/10.1002/9781118704417.ch7

Raeder, J., Cramer, W. D., Jensen, J., Fuller-Rowell, T., Maruyama, N., Toffoletto, F., & Vo, H. (2016). Sub-Auroral Polarization Streams: A complex interaction between the magnetosphere, ionosphere, and thermosphere. *Journal of Physics: Conference Series*, *767*, 012021. https://doi.org/10.1088/1742-6596/767/1/012021

Richmond, A. D., Ridley, E. C., & Roble, R. G. (1992). A thermosphere/ionosphere general circulation model with coupled electrodynamics. *Geophysical Research Letters*, *19*(6), 601–604. https://doi.org/10.1029/92GL00401

Sandel, B. R., King, R. A., Forrester, W. T., Gallagher, D. L., Broadfoot, A. L., & Curtis, C. C. (2001). Initial results from the IMAGE Extreme Ultraviolet Imager. *Geophysical Research Letters*, *28*(8), 1439–1442. https://doi.org/10.1029/2001GL012885

Schunk, R. W., Banks, P. M., & Raitt, W. J. (1976). Effects of electric fields and other processes upon the nighttime high-latitude *F* layer. *Journal of Geophysical Research*, *81*(19), 3271–3282. https://doi.org/10.1029/JA081i019p03271

Tian, X., Yu, Y., Zhu, M., Ma, L., Cao, J., Pr, S., et al. (2022). Effects of EMIC Wave-Driven Proton Precipitation on the Ionosphere. *Journal of Geophysical Research: Space Physics*, *127*(2). https://doi.org/10.1029/2021JA030101

Toffoletto, F., Sazykin, S., Spiro, R., & Wolf, R. (2003). Inner magnetospheric mod- eling with the rice convection model. *Space Science Reviews*, *107*(1/2), 175–196. https://doi.org/10.1023/A:1025532008047

Wang, W., Talaat, E. R., Burns, A. G., Emery, B., Hsieh, S., Lei, J., & Xu, J. (2012). Thermosphere and ionosphere response to subauroral polarization streams (SAPS): Model simulations: THE EFFECT OF SAPS ON THE T-I SYSTEM. *Journal of Geophysical Research: Space Physics*, *117*(A7), n/a-n/a. https://doi.org/10.1029/2012JA017656

Wolf, R. A. (1983). The Quasi-Static (Slow-Flow) Region of the Magnetosphere. In R. L. Carovillano & J. M. Forbes (Eds.), *Solar-Terrestrial Physics* (Vol. 104, pp. 303–368). Dordrecht: Springer Netherlands. https://doi.org/10.1007/978-94-009-7194-3_14

Zhang, B., Lotko, W., Brambles, O., Wiltberger, M., & Lyon, J. (2015). Electron precipitation models in global magnetosphere simulations. *Journal of Geophysical Research: Space Physics*, *120*(2), 1035–1056. https://doi.org/10.1002/2014JA020615

Zhang, Binzheng, Sorathia, K. A., Lyon, J. G., Merkin, V. G., Garretson, J. S., & Wiltberger, M. (2019). GAMERA: A Three-dimensional Finite-volume MHD Solver for Non-orthogonal Curvilinear Geometries. *The Astrophysical Journal Supplement Series*, *244*(1), 20. https://doi.org/10.3847/1538-4365/ab3a4c

Zou, S., Ridley, A. J., Moldwin, M. B., Nicolls, M. J., Coster, A. J., Thomas, E. G., & Ruohoniemi, J. M. (2013). Multi-instrument observations of SED during 24-25 October

2011 storm: Implications for SED formation processes: SED FORMATION PROCESSES. *Journal of Geophysical Research: Space Physics*, *118*(12), 7798–7809. https://doi.org/10.1002/2013JA018860

Zou, S., Moldwin, M. B., Ridley, A. J., Nicolls, M. J., Coster, A. J., Thomas, E. G., & Ruohoniemi, J. M. (2014). On the generation/decay of the storm-enhanced density plumes: Role of the convection flow and field-aligned ion flow: Generation and Decay of SED Plumes. *Journal of Geophysical Research: Space Physics*, *119*(10), 8543–8559. https://doi.org/10.1002/2014JA020408

Zou, Y., Walsh, B. M., Shi, X., Lyons, L., Liu, J., Angelopoulos, V., et al. (2021). Geospace Plume and Its Impact on Dayside Magnetopause Reconnection Rate. *Journal of Geophysical Research: Space Physics*, *126*(6). https://doi.org/10.1029/2021JA029117

The relation among the ring current, subauroral polarization stream, and the geospace plume: MAGE Simulation of the March 31 2001 Super Storm

Shanshan Bao[1], Wenbin Wang[2], Kareem Sorathia[3], Viacheslav Merkin[3], Frank Toffoletto[1], Dong Lin[2], Kevin Pham[2], Jeffrey Garretson[3], Michael Wiltberger[2], John Lyon[4] and Adam Michael[3]

[1]Department of Physics and Astronomy, Rice University, Houston TX

[2]High Altitude Observatory, National Center for Atmospheric Research, Boulder CO

[3]Applied Physics Laboratory, Johns Hopkins University, Laurel MD

[4]Department of Physics and Astronomy, Dartmouth College, Hanover NH

Corresponding author: Shanshan Bao (shanshan.bao@rice.edu)

Key Points:

- The first whole geospace simulation to demonstrate coherent storm-time evolution of plasmaspheric and total electron content (TEC) plumes.
- The model demonstrates plasmasphere erosion and TEC depletion by the subauroral polarization streams (SAPS).
- SAPS is sustained by magnetospheric ion and electron distributions formed by a delicate balance of energy-dependent and **E**×**B** drifts.

Abstract

The geospace plume, referring to the combined processes of the plasmaspheric and the ionospheric storm-enhanced density (SED)/total electron content (TEC) plumes, is one of the unique features of geomagnetic storms. The apparent spatial overlap and joint temporal evolution between the plasmaspheric plume and the equatorial mapping of the SED/TEC plume indicate strong magnetospheric-ionospheric coupling. However, a systematic modeling study of the factors contributing to geospace plume development has not yet been performed due to the lack of a sufficiently comprehensive model including all the relevant physical processes. In this paper, we present a numerical simulation of the geospace plume in the March 31, 2001 storm using the Multiscale Atmosphere Geospace Environment model. The simulation reproduces the observed linkage of the two plumes, which, we interpret as a result of both being driven by the electric field that maps between the magnetosphere and the ionosphere. The model predicts two velocity channels of sunward plasma drift at different latitudes in the dusk sector during the storm main phase, which are identified as the sub-auroral polarization stream (SAPS) and the convection return flow, respectively. The SAPS is responsible for the erosion of the plasmasphere plume and contributes to the ionospheric TEC depletion in the midlatitude trough region. We further find the spatial distributions of the magnetospheric ring current ions and electrons, determined by a delicate balance of the energy-dependent gradient/curvature drifts and the E×B drifts, are crucial to sustain the SAPS electric field that shapes the geospace plume throughout the storm main phase.

1 Introduction

During geomagnetically active times, multiscale dynamic processes are triggered throughout the magnetosphere, the ionosphere and the thermosphere in response to the solar wind driving. Once the global magnetospheric convection initiates, the ring current starts to accumulate, reshaping the global structure of the magnetosphere and establishing a distinctive dynamic storm-time pattern of the electromagnetic field and plasmas. The Imager for Magnetopause-to Aurora Global Exploration (IMAGE) satellite observed the dynamic evolution of the cold (~1eV) and dense (~ 10^4/cc) plasmasphere (Lemaire et al., 1998) and the sunward extension of a plume-like high density structure from the dusk edge of the plasmasphere (the "drainage plume") through the EUV images (Burch et al., 2001; Sandel et al., 2001; Goldstein, 2004; Goldstein & Sandel, 2005). The IMAGE satellite also detected, through the high-energy neutral atom (HENA) images, that the spatial distribution of the partial ring current roughly complements the shape of the plasmapause (Pulkkinen et al., 2005; Goldstein, 2007). In the ionosphere, the storm-time electron density enhancement at low to midlatitudes in the day and dusk sectors is a prominent feature known as a "positive storm effect" (Liu et al., 2016; Fagundes et al., 2016). Furthermore, a plume-like high total electron content (TEC) structure extends from the positive storm effect region in the noon-to-dusk sector toward higher latitudes and into the polar cap, which is commonly observed by incoherent scatter radars, ground-based Global Positioning System (GPS) measurements and near-Earth satellites (e.g., Foster, 1993; Zou et al., 2013, 2014; Foster et al., 2020). The term "geospace plume" has been used to refer to the coupled, jointly evolving high plasma density structures including the plasmaspheric drainage plume and the storm-enhanced density (SED)/TEC plume in the ionosphere (Foster et al., 2020). Foster et al. (2002) first pointed out the "linkage" between the plasmaspheric plume and the ionospheric SED/TEC plume by comparing the IMAGE EUV plasmasphere image and the equatorial mapping of the GPS TEC map. They noted that the co-location of the plumes indicates strong magnetosphere-ionosphere (MI) coupling. Further observations show that the sub-auroral polarization stream (SAPS), a latitudinally narrow large plasma drift channel in the sub-auroral ionosphere in the dusk-to-midnight sector (Foster & Burke, 2002), may play an important role in shaping the dusk edge of the plasmasphere and further depleting the middle latitude electron density trough in the ionosphere. In other words, the SAPS electric field maps across the plasmapause on the dusk side causing strong westward ion transport and contributes to the formation of the ionospheric electron density trough which is co-located with the SAPS channel (Foster & Burke, 2002; Foster, 2002; Foster et al., 2007, 2014; Zou et al., 2021).

Numerical simulations of the geospace plume system have been conducted along with the observational studies. Goldstein et al. (2003, 2005, 2014) used cold test particles at the plasmapause that were driven by empirical convection and an ad-hoc SAPS electric potential to track the plasmasphere evolution. They found that the SAPS electric field is crucial in order to reproduce the storm-time, dusk-side structures of the plasmasphere, such as the plasmapause radius and the plasmaspheric plume. The first 3D simulation of the plasmasphere was conducted using the SAMI3 model that was driven by an empirical electrostatic potential (Huba & Krall, 2013). The study found that the simulated plasmasphere evolves from a toroidal symmetric shape into a contracted size with a development of a plume-like structure after the storm. The Thermosphere Ionosphere Electrodynamics General Circulation Model (TIEGCM) (Richmond et al., 1992; Qian et al., 2014) has been extensively used to investigate thermosphere-ionospheric response to geospace disturbances and SAPS. For example, C. H. Lin et al. (2005) used the TIEGCM with the $\mathbf{E}\times\mathbf{B}$ drift derived from satellite measurements of the ion velocity to study the relative importance of winds and electric field for low and midlatitude electron density enhancements. Wang et al. (2012) and Lu et al. (2020) used a synthetic SAPS electric field model to investigate the response of neutral winds, SED plume and traveling ionospheric disturbances to SAPS. SAMI3 coupled with the Rice Convection Model (RCM) of the inner magnetosphere was used to simulate the evolution of the ionosphere-plasmasphere system and demonstrated the linkage between the plamaspheric plume and the mapped SED/TEC plume during a geomagnetic storm (Huba & Sazykin, 2014, 2017).

In recent years, magnetosphere-ionosphere-thermosphere (M-I-T) coupled models have been developed and used to simulate SAPS (Raeder et al., 2016; Lin et al., 2019, 2021, 2022). These studies showed that the coupled geospace models can capture the complex interactions and feedback loops in the M-I-T system and reproduce the distinctive features of SAPS in observations. Yet, such coupled models have not yet been used to study the geospace plume. Most of the previous modeling studies simulated the plasmaspheric plume and the ionospheric SED/TEC plume separately, precluding studies that would elucidate the physics underlining the linkage between the two plumes. The use of ad-hoc or empirical SAPS electric field instead of self-consistent, physics-based SAPS modeling prevents an investigation of the magnetosphere-ionospheric coupling processes involved, where the coupled processes of the ring current buildup, the Region-2 current generation and the electron precipitation could play important roles in the generation of SAPS (Lin et al., 2021, 2022) and the plume dynamics. SAMI3-RCM simulation (Huba & Sazykin, 2014, 2017) had the advantage of a common electromagnetic field driving both ionospheric and magnetospheric plumes in the closed-field-line region, but it lacked a physics-based representation of high-latitude dynamics coupled to the rest of the simulation domain and an outer-magnetosphere model that can provide the ring current model with storm-time plasma injections at its boundary (Bao et al., 2021; Cramer et al., 2017; De Zeeuw et al., 2004; Lin et al., 2021; Pembroke et al., 2012).

In this study, we use such a coupled M-I-T model to gain a comprehensive understanding of the geospace plume evolution during storm-times. We address three science questions: (1) What is the cause of the linkage between the plamaspheric plume and the ionospheric SED/TEC plume? (2) What specific processes are important for shaping the geospace plume? (3) What is the relation between the ring current build-up and the geospace plume development? For this purpose, we employ the Multiscale Atmosphere-Geospace Environment (MAGE) model (Lin et al., 2021, 2022; Pham et al., 2022) to simulate the multiscale dynamics throughout the outer and inner magnetosphere, the ionosphere and the thermosphere to determine the relevant correlations and potential causal relationships. The coupled whole geospace model requires a number of key components. First is the global magnetospheric MHD model that can capture both global and inner magnetospheric dynamics such as large-scale storm-time magnetospheric convection and particle gradient/curvature drifts and provide self-consistent dynamic magnetic field configuration along with the associated current system. A coupled thermosphere-ionospheric model is also needed to not only self-consistently evolve the upper atmospheric neutral species but also simulate ionospheric electron densities, and provide ionospheric conductance to solve the current continuity equation for the global ionospheric electrostatic potential. Finally, the model must include the coupling of FACs, particle precipitation, ionospheric conductance, and ionospheric electric field to ensure feedback and self-consistency within the entire geospace system.

2 The MAGE model

The MAGE model used in this study provides a comprehensive and self-consistent description of multiscale physical processes in the different domains of geospace. The current version of MAGE (1.0) couples the global magnetosphere, the inner magnetosphere, the ionosphere and the thermosphere (Lin et al., 2021, 2022; Pham et al., 2022). As shown in Figure 1, the global magnetospheric MHD model, Grid Agnostic MHD with Extended Research Applications (GAMERA) model (Zhang et al., 2019; Sorathia et al., 2020) solves the single-fluid MHD equations and passes FACs to the ionosphere potential solver, and the RE-developed Magnetosphere-Ionosphere Coupler/Solver (REMIX) which is a rewrite of the Magnetosphere-Ionosphere Coupler/Solver (MIX) code (Merkin & Lyon, 2010). REMIX solves the electric potential for both hemispheres. The GAMERA plasma moments and electromagnetic field are passed to the Rice Convection Model (RCM), the inner magnetosphere ring current model (Toffoletto et al., 2003), to evolve the drifting plasma distribution in the form of multiple-fluids with different energy invariants. The plasmasphere is modeled as a zero-energy proton channel in RCM and follows the $\mathbf{E}\times\mathbf{B}$ drift including corotation. The plasmasphere is initialized with a 2D density profile as a function of the Kp index modified from the 1D Gallagher model (Gallagher et al., 2000). The total plasma density and pressure are fed back to the GAMERA model. There are also two kinds of electron precipitation simulated by the current MAGE model: the RCM-computed diffuse electron precipitation, i.e., pitch-angle scattered electrons falling into the loss cone (Wolf, 1983; Bao, 2019), and the GAMERA-computed mono-energetic electron precipitation accelerated by field-aligned potential drops (Zhang et al., 2015). The electron precipitation and the electric potential are used as input to the TIEGCM that calculates the density, temperature and transport of electrons, ions, and neutrals. The electron precipitation, along with the solar EUV radiation, produces ionization in the ionosphere and the ionospheric conductivity.

Two important physical processes are not yet included in MAGE and therefore are not addressed in this study. The first is a physics-based representation of the plasmaspheric refilling process. In the current version of MAGE, we model the plasmasphere inside the inner-magnetosphere model, RCM, with a simple empirical refilling model being used, whereas the ionospheric electron density is solved separately in a coupled thermosphere-ionospheric model, TIEGCM. Specifically, in this study, the refilling model is in fact turned off to isolate the effects of electrodynamic coupling and investigate whether the linkage of the two plumes still exists without mass exchange. Plasmasphere refilling is a slow process (~ days) compared with the storm-time plasmaspheric density changes (~ hours) (Lawrence et al., 1999; Denton et al., 2012; Krall et al., 2014) and the exclusion of the refilling should not fundamentally change the storm-time plasmaspheric dynamics.

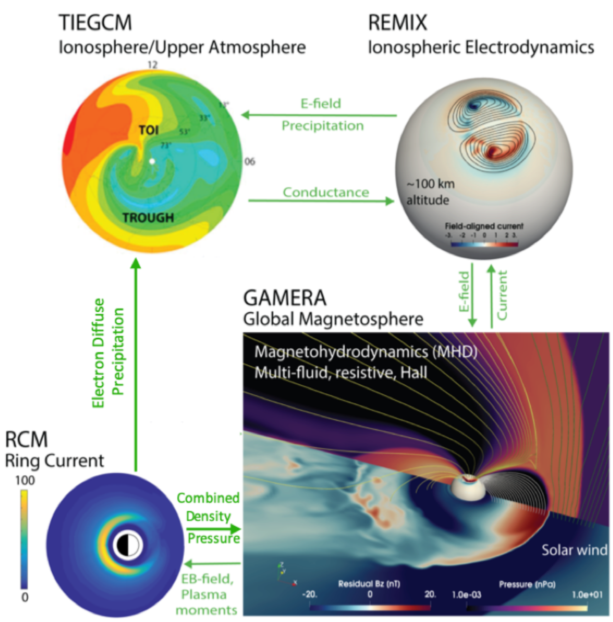

Figure 1. Diagram of the MAGE components and their coupling in this study.

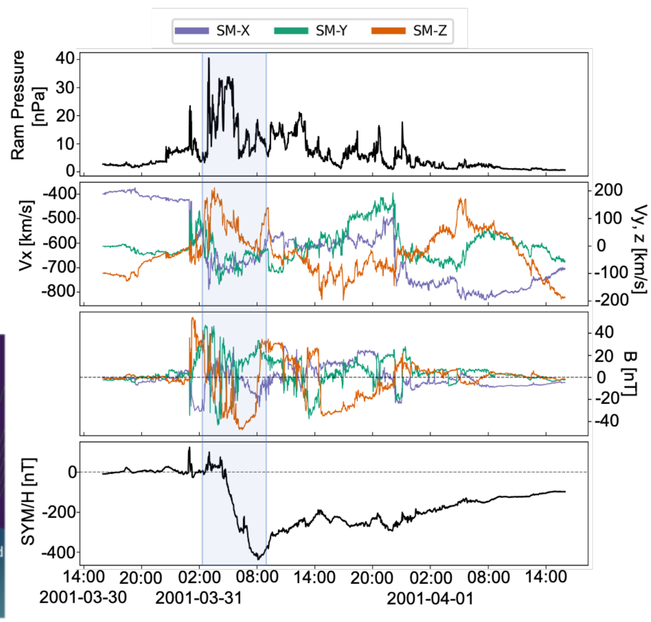

Figure 2. Solar wind dynamic pressure and velocity (top two panels), IMF components (third panel), and the SYM-H index (bottom panel) during the March 31, 2001, super storm. Data source: CDAWeb/NASA

2.1 Simulation Setup

The event studied in the paper is the super storm that occurred on March 31, 2001. The super storm was a result of a coronal mass ejection event that caused the SYM/H index to reach -400 nT. Figure 2 shows the solar wind profile, including, from top to bottom, the dynamic ram pressure, the solar wind velocity components, the interplanetary magnetic field (IMF) components, and the SYM/H index, extracted from the NASA/GSFC's OMNI dataset through CDAWeb. There are two periods of southward (SW) IMF, the first, 03:00~08:00UT 03-31-2001, which was followed by a period of northward IMF, and the second, 15:00~22:00UT. The simulation covered the entire storm, but our analysis focuses mostly on the geospace plume development in the first period of the southward IMF (highlighted in Figure 2 in blue shade).

In this work, we use the so called 'Quad' resolution for GAMERA, which corresponds to 96, 96, and 128 grid cells in radial, meridional and azimuthal directions (the spherical axis of the grid is aligned with the Solar Magnetic (SM) x-axis). The non-uniform 3D grid is much denser in the inner magnetosphere region with its inner boundary set at 1.5R_E. The REMIX 2D grid is 1°×1° in longitude and latitude with a low latitude boundary at 35° magnetic latitude (MLAT). The RCM 2D physical grid is 1°×1/3° in longitude and latitude and for the energy grid, it uses 1 energy channel for the plasmasphere, 29 energy channels for the electrons and 84 energy channels for the protons. Oxygen channels are not used in this study. GAMERA, REMIX and RCM grids are defined in the SM coordinates. The TIEGCM 3D grid covers the entire globe and is defined in the geographic coordinates. Its resolution is 1.25°×1.25° in longitude and latitude and it has 57 levels of vertical pressure grid (1/4 scale height resolution), ranging from ~97 km to approximately 900 km. The coupling exchange interval between GAMERA and REMIX is 5 s, while for GAMERA and RCM, the exchange interval is 15 s and for REMIX and TIEGCM, it is 5 s. The MAGE simulation starts at 16:00 UT, March 30, 2001 and lasts for 48 hours.

3. Overview of the simulation results

The evolution of the geospace plume is shown in Figure 3 through different stages of the storm (specifically for the 1st period of the southward IMF in Figure 2). The entire process of geospace plume development is demonstrated in Movies S1 and S2. In Figure 3(a1)-(a5) (the first row) and (d1)-(d5) (the fourth row), we map the relevant processes onto the magnetic equatorial plane defined as the surface of minimum magnetic field. The plasmapause as the 100/cc iso-surface of the cold proton density. The colored areas are within the closed-field-line region and the blanked areas are for the open-field-line region. The electric potential ϕ plotted in the equatorial plane is a combination of the ionospheric electrostatic potential ϕ_I and the corotation potential ϕ_c, defined as

$$\phi = \phi_I + \phi_c \tag{1}$$

$$\phi_c = -\frac{\omega_E B_0 R_E^3}{r} \tag{2}$$

where r is the radial distance; ω_E is the angular speed of the Earth's rotation; B_0 is the strength of the Earth's dipole moment; R_E is the radius of the Earth (Toffoletto et al., 2003). The contours of the electric potential represent the streamlines of the plasma **E**×**B** drift flow. Here, the ionospheric electrostatic potential ϕ_I is calculated by REMIX and shown in Figure 3(b1)-(b5) (the second row). The ionospheric potential calculated by TIEGCM is shown in Figure(c1)-(c5) (the third row), where it uses the electric potential from REMIX in the high latitude region (MLAT > 60) and solves for global ionospheric potential including the neutral wind dynamo. All the ionospheric plots in this paper are for the northern hemisphere.

At the pre-storm stage (Figures 3(a1)-(d1), the first column), both the FACs and the ionospheric electric potential are weak. The co-rotation electric field dominates and drives the plasmasphere co-rotate with the Earth, with the plasmapause around 3.5~4R_E (bottom row, Figure 3(d1) The ionospheric TEC peaks near 20 MLAT with a value of ~140 TECu and has a higher value (>50TECu) in the noon-to-dusk sector from low- to midlatitude than in the midnight-to-dawn sector.

Around 02:30~04:30UT, 03-31-2001, the impact of the CME event arrives at Earth, with an evident increase in the ram pressure and fluctuations in the IMF (Figure 2) causing the storm initial phase. By the end of the initial phase (Figure 3(a2)-(d2), the second column) the solar wind driving has caused the formation of the Region-1 current, while the Region-2 current is still relatively weak. The two-cell convection pattern in the electric potential starts to establish and this initiates global-scale sunward convection on the nights side (Figure 3(b2)), although the ring current has not yet developed (Figure 3(a2)). From the extent of the dashed contour lines of the potential in Figure 3(d2), we can see that a plume-like structure began to emerge in the plasmasphere as well as in the middle-high latitude ionosphere. Specifically, the plasmasphere starts to expand sunward and a finger-like structure (a plasmaspheric "finger") starts to develop at the dusk edge of the plasmapause (heavy line in Figure 3(d2)). We will briefly discuss its cause in Section 4.2.1.

During the early main phase (Figure 3(a3)-(d3), the third column), the FACs and the ionospheric convection electric fields become stronger (Figure 3(b3)). The Region-2 current is enhanced due to a substantial ring current pressure accumulation (Figure 3(a3)). The peak of the TEC has moved to 30 MLAT and a TEC plume occurs with ~70TECu and expands toward the polar cap from 45 MLAT to 75 MLAT near 14 MLT driven by the dusk-cell of the convection (Figure 3(c3)). The plasmaspheric plume has formed, with the plasmasphere finger merged into its main body (Figure 3(d3)). The shape of the plasmaspheric plume maintains approximate dawn-dusk symmetry about the noon-midnight line in the equatorial plane.

In the late main phase (Figure 3(a4)-(d4), the fourth column), the strength of the ring current reaches its maximum. Due to the westward drifting of the ion population, the ring current pressure distribution is skewed toward pre-midnight (Figure 3(a4)). The FACs become much more intense (Figure 3(b4)) causing stronger central convection electric field that enhances the ionospheric-poleward/equatorial-sunward expansion of the geospace plume (Figure 3(b4), (c4) and (d4)). The high TEC region due to the positive storm effect extends from 30 MLAT to 45 MLAT and 60 MLAT in the ionosphere (Figure 3(c4)) and it becomes the center of the TEC plume on the equatorial plane (Figure 3(d4)). Meanwhile, the two-cell convection pattern is skewed clockwise, where the dusk-side pair of the Region-1 and the Region-2 current is located mostly in the afternoon sector and the dawn-side pair of the Region-1 and Region-2 current is skewed to the pre-dawn sector (Figure 3(b4)). The clockwise twist of the convection pattern reshapes the geospace plume. As shown in Figure 3(d4), the shape of the plasmasphere and the TEC contour follows the shape of the potential contour lines. The potential contours show a prominent dawn-dusk asymmetry. As positive storm effects occur primarily in the late afternoon to dusk (~14-19 MLT in Figure 3(c4)) at low and middle latitudes, the strong convection in the dusk sector transport plasma toward high latitudes. The plume structure follows the potential contours and the plume is biased to the dusk side. Another prominent feature during the main phase is the presence of TEC depletion channels. In the dusk sector, a low TEC channel expands from the equator and merges into the midlatitude (~45 MLAT) electron density/TEC trough region. There is another low-TEC channel located around 60 MLAT inside the auroral oval. Both TEC depletion channels (marked by red arrows in Figure 3(c4)) extend sunward. In the equatorial plane, the midlatitude depletion channel is located at the dusk edge of the plasmaspheric plume and we can see the plasmaspheric plume has become much narrower compared with its shape in the early main phase. We refer to this depletion of the TEC and the narrowing of the plasmaspheric plume as geospace plume “erosion”. We will discuss these two features in Sections 4.2.2.

In the last stage, 08:00~12:00UT, 03-31-2001, which is the storm recovery phase (Figure 3(a5)-(d5), the fifth column), the IMF turns northward and the ram pressure decreases. The ionospheric convection becomes much weaker (Figure 3(b5)). The two TEC depletion channels merge into one and cut across the tongue of ionization and leaves some polar cap patches (Figure 3(c5)). In the equatorial plane (Figure 3(d5)), the sunward driving of the plasmaspheric plume diminishes and the co-rotation takes over again. Due to the loss of the particles through the dayside to the open-field-line region, the size of the plasmasphere shrinks significantly with a plasmapause radius of 2 ~ 2.5R_E.

There are three prominent features from the simulation results. The first is that the equatorial plane mapping of the TEC colored contour resemble the shape of the plasmapause. Especially during the storm's main phase, their synchronized sunward expansion and the overlap of the two plumes is quite apparent. We will discuss the major cause of their linkage in Section 4.1. The second feature, as mentioned above, is the density depletion channels in the dusk sector at midlatitude. We investigate their role in eroding the dusk edge of the plasmasphere plume in Section 4.2. Thirdly, the ring current development with its dusk-preferred accumulation significantly impacts the distribution of the FACs and thus the electric fields, which eventually control to the geospace plume development. We investigate the relation between the ring current build-up and the geospace plume evolution in detail in Section 4.3.

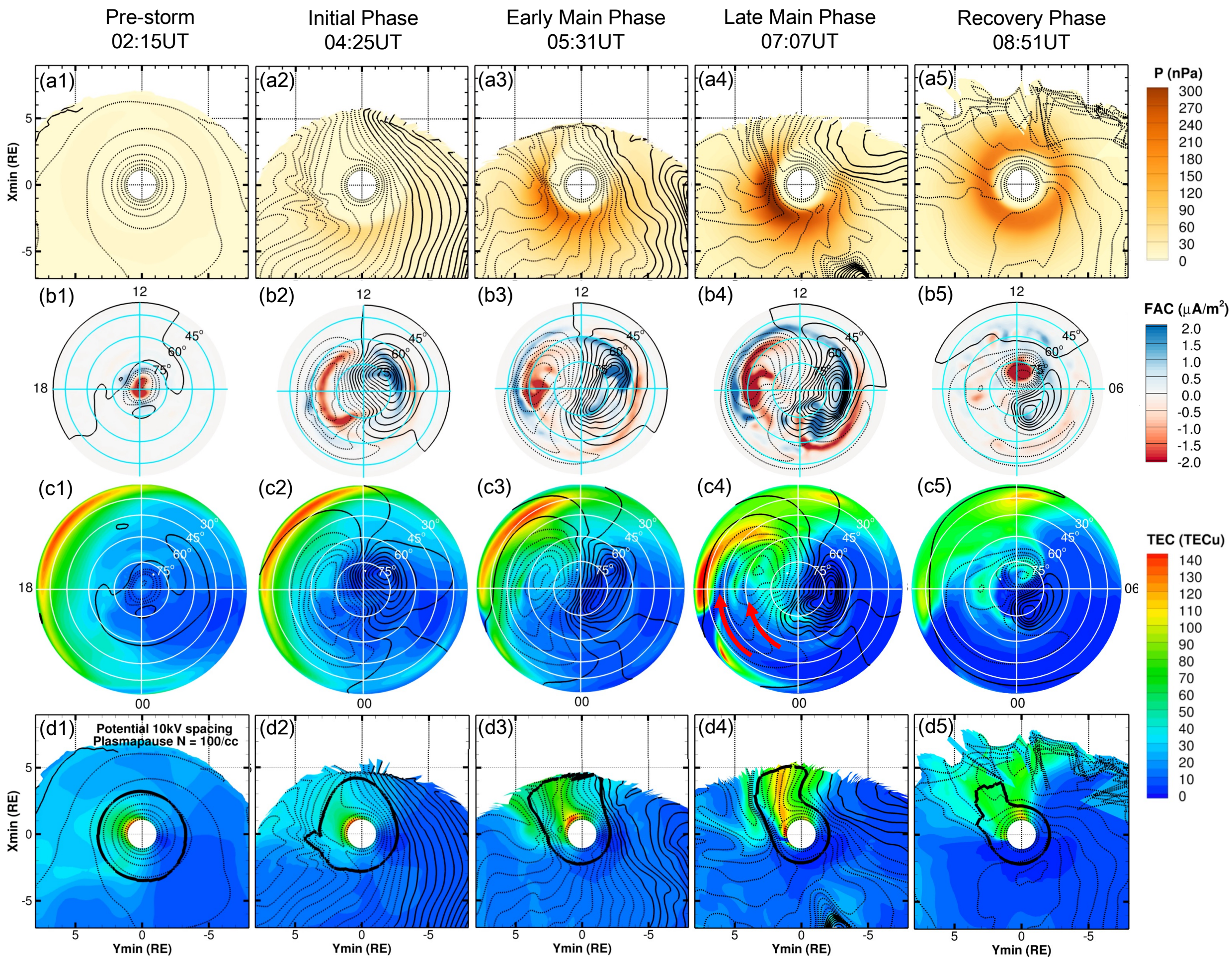

Figure 3. (a1)-(e1) to **(a5)-(e5)** show five stages of the storm (the 1st period of southward IMF shaded in Figure 2) with each column, top to bottom, depicting the equatorial plane view of the ring current pressure, the ionospheric FAC, the ionospheric TEC and the equatorial plane mapping of the TEC and the plasmapause (heavy black contour). The thin black lines (dashed for negative values) are contours of the electric potential, with 10keV interval on equatorial plane (bottom row) and 20keV in the ionosphere (third row from top).

4. Discussion

4.1 Linkage between the plasmaspheric and the ionospheric plumes

Foster et al. (2002) first reported the overlap of the plasmaspheric plume with the magnetospheric mapping of the ionospheric plume during the March 31, 2001 storm. The IMAGE satellite and the World-wide TEC measurement jointly observed the resemblance of the two plumes for the second period of the southward IMF. Figure 4(a) shows the IMAGE EUV image of the plasmasphere at 21:23UT, March 31, 2001 (Source: http://euv.lpl.arizona.edu/euv/). Figure 4(b) is the World-wide TEC data (Source: Madrigal database) mapped to the equatorial plane using the magnetic field-line traced in the MAGE model. Figures 4(a) and (b) are adjusted to a similar length scale as Figure 4 of Moldwin et al., 2016. The plasmapause is located at approximately $2R_E$ on the nightside and the plasmaspheric drainage plume expands from the dusk edge of the plasmasphere toward the subsolar magnetopause (Figure 4(a)). The projection of the observed global TEC on the equatorial plane at 21:22UT (Figure 4(b)) shows similar shape and orientation with the plasmaspheric plume. Figure 4(c) gives the MAGE simulated plasmapause and TEC projected to the equatorial plane on the same color scale. The simulated plasmaspheric plume is co-located with the TEC plume which is consistent with the observations.

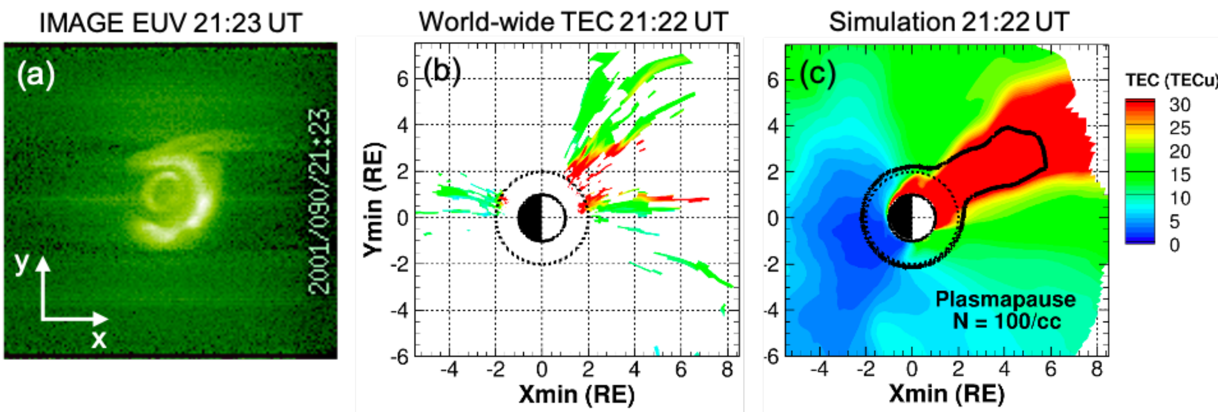

Figure 4. (a) IMAGE EUV image of the plasmasphere taken at 21:23UT, 03-31-2001. **(b)** The equatorial-plane projection of the global TEC measurement at 21:22UT, 03-31-2001, mapped by the MAGE magnetic field line. **(c)** The contour plot of the MAGE simulated plasmapause and TEC projection on the equatorial plane. The plasmasphere and the TEC are presented in SM coordinates. The sun is to the right. Black solid circle represents the Earth and the dashed black circle has a radius of $2R_E$.

This overlap in the equatorial mapping of the two plumes can be seen throughout the storm. As described in Section 3 and shown in Figure 4, both the plasmasphere and the electron content co-rotate eastward when the two-cell potential pattern has not yet been established. During the strong southward IMF driving, e.g., at T = 650 ~ 950 min in Movie S1, the ionospheric two-cell convection dominates over the co-rotation. The evolution of the plumes is controlled by the dusk cell and follows the geometry of local electric potential contours. In the noon-to-dusk sector, the plumes extend from the low middle latitudes to the pole, which corresponds to the sunward expansion in the equatorial plane.

Compared to the SAMI3-RCM simulation of the same event (Huba & Sazykin, 2014), in our MAGE simulation, the plasmaspheric plume (from RCM) and the TEC (from TIEGCM) plume are driven by the midlatitude electric fields that are controlled by the same high-latitude electric field, but the mass exchange between the ionosphere and the plasmasphere is not included. However, the overlap and joint evolution of the two plumes are still successfully reproduced. This indicates that the electrodynamic coupling in the M-I-T system, rather than the mass connection, plays a dominant role in the formation and evolution of the geospace plume in both the plasmasphere and the ionosphere.

4.2 Westward ion drifts (WIDs) and their effect on the geospace plume

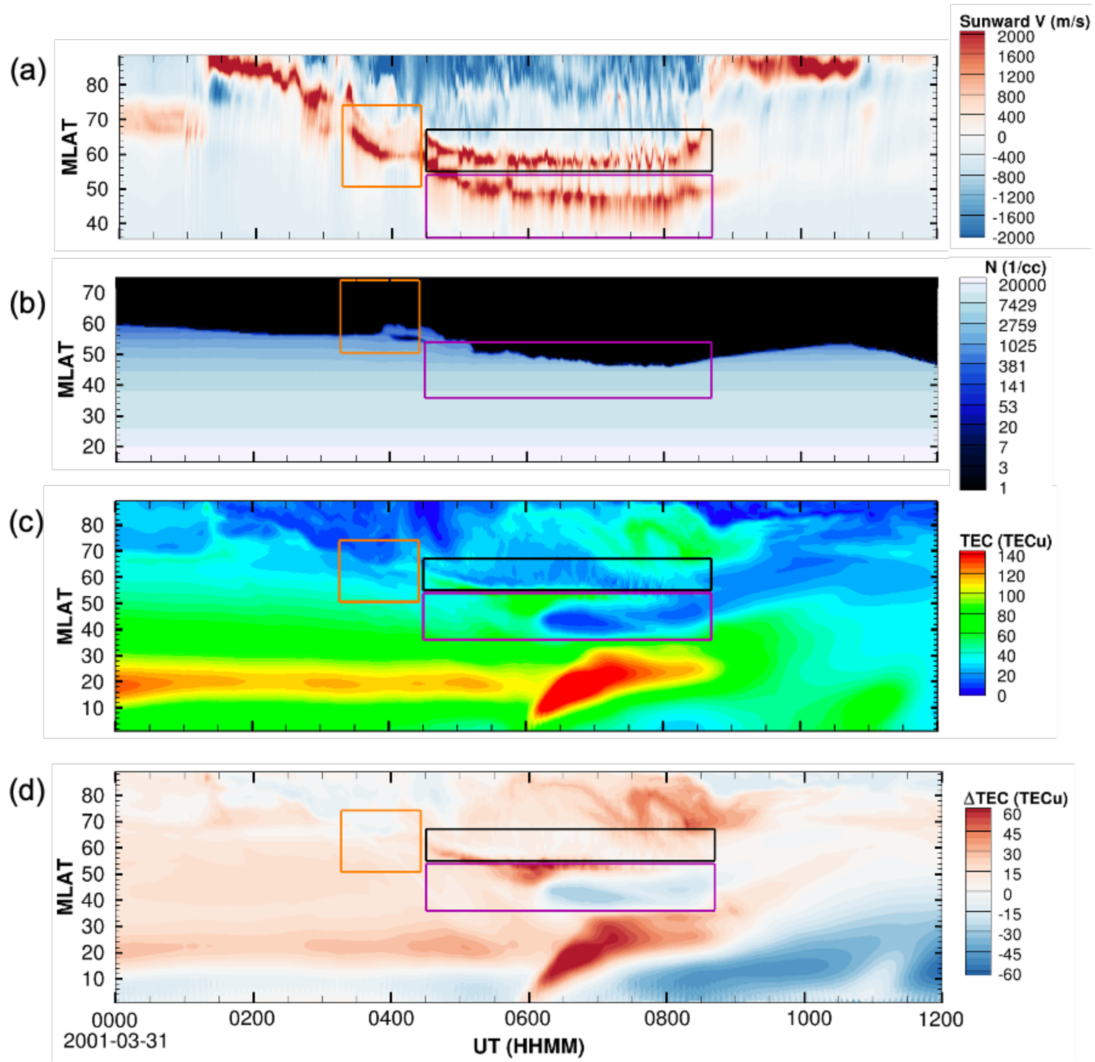

Figure 5. (a)-(d) Keograms of the simulated westward (sunward) ion drift velocity, plasmaspheric density, TEC and ΔTEC at 18 MLT. ΔTEC is calculated by subtracting the quiet-time (March 29, 2001) TEC from the storm-time TEC at the same UT. The colored boxes mark the sunward velocity peaks and the corresponding erosion region in the plasmaspheric density, TEC and ΔTEC. The boxes of the same color cover the same range of latitude in different panels. The orange box marks the WID in the initial phase; the purple box marks the WID velocity peak in the midlatitude; the black box marks the?????

To further investigate the geospace plume erosion on the dusk side, we sample the MAGE simulated ion drift velocity (from REMIX), ionospheric mapping of the plasmaspheric density (from RCM), TEC and ΔTEC (from TIEGCM) along 18 MLT for the first period of southward IMF (Figures 5(a) - (d)). The Y-axes of different panels cover different ranges of magnetic latitude since the variables are calculated in different MAGE component models. In Figure 5(a), the ion drift velocity is a combination of the corotation velocity and the **E**×**B** ion drift velocity in the SM coordinates. The red color signifies a westward (i.e., sunward at 18 MLT) direction, while the blue color signifies an eastward/tailward direction.

4.2.1 The plasmasphere finger

During the initial phase (around 01:30~04:30UT), when the two-cell convection pattern starts to establish, a single band of WID velocity peak moves from high latitude toward midlatitude (Figure 5(a)). A weak reduction in the TEC can be seen at the similar MLAT according to Figures 5(c) and (d). When the WID peak extends to 60 MLAT, it reaches the plasmapause and drives the expansion of a plasmasphere finger (Figure 5(b)), a f. The orange box in Figure 5(b) marks the period of finger development in the initial phase (T = 705~750 min in Movie S1) and Figure 6 shows a snapshot of the finger-like structure that develops at the dusk edge of the plasmapause and expands radially following the electric potential contour (marked by the orange arrows) at 04:24 UT. We can see from Figure 6 that the cause of the plasmaspheric finger is a result of the interaction between the plasmapause which is around 3.5 ~ 4R_E at the early stage of the storm and the equatorward-expanding dusk convection cell of the electric field.

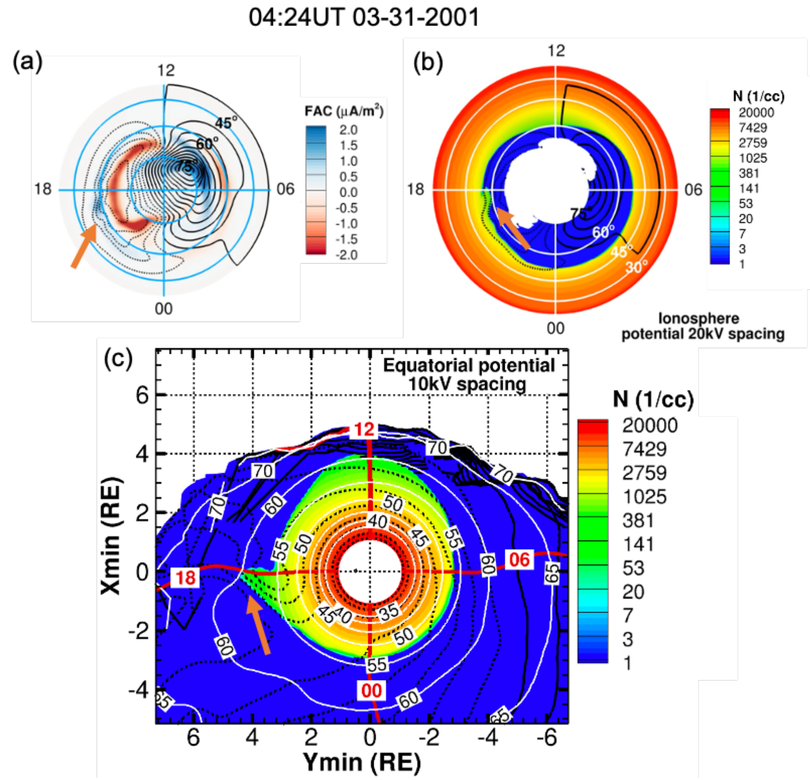

Figure 6. (a)-(c) Snapshots taken at 04:24UT 03-31-2001 at the end of the initial phase. **(a)** Simulated FAC in SM coordinates. **(b)** and **(c)** are ionospheric mapping and equatorial plane view of the plasmaspheric density with contour lines of the indicated MLT (red) and latitude (white) mapped to the plane. Black contour lines in **(a-b)** and **(c)** show electric potential with 20kV and 10kV intervals respectively, dashed for negative values. The orange arrows point to the location of the enhanced electric fields and the plasmasphere finger between 55 to 60 MLAT during the initial phase, which correspond to the westward drift velocity peak marked in Figure 5(a) by the box of the same color.

4.2.2 Erosion on the geospace plume

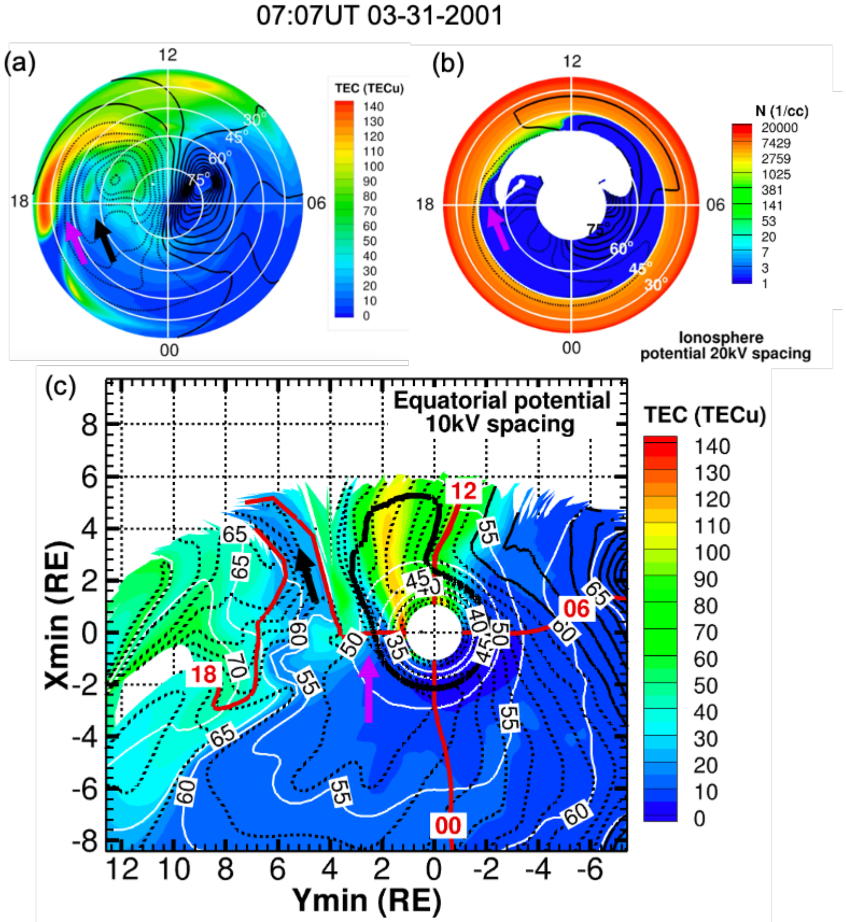

Figure 7. (a)-(c) Snapshots taken at 07:07UT 03-31-2001 in the late main phase. **(a)** Simulated TEC in SM coordinate. **(b)** and **(c),** same variables as in Figure 6. The purple and black arrows point to the locations of the density depletion, which correspond to the SAPS channel and the CRF marked in Figure 5 by the box of the same colors.

During the main phase (around 04:30~8:10UT, T = 750~970 min in Movie S1), the two-cell convection pattern has established, double-band WID velocity peaks appear (Figure 5(a)), with one peak located at higher latitudes around 60 MLAT marked by the black box and another located at midlatitudes around 45~50 MLAT marked by the purple box. As shown in Figure 5(b), the plasmapause in the purple box moves from 55 MLAT to 45 MLAT. The velocity peak around 60 MLT does not overlap with the plasmasphere and thus, cannot directly interact with and influence it. In Figure 5(c), two large WID velocity channels are collocated with regions of low TEC, which can be seen in both black and purple boxes. The TEC depletion effect along with the midlatitude subauroral velocity peak is much more prominent according to Figure 5(d), where the depletion in TEC and ionospheric electron densities is quite obvious. However, ΔTEC in the black box does not show a negative value, which means the decrease of the TEC around 60 MLAT may not be an obvious storm effect. Figure 7 shows the snapshots of TEC depletion and the plasmaspheric erosion corresponding to the double-band WID velocity channels (marked by the black and purple arrows). Figure 7(c) demonstrates clearly that in the equatorial plane, the midlatitude velocity peak (purple arrow) is collocated with TEC depletion and erodes the dusk edge of the plasmaspheric plume, while the higher latitude velocity peak (black arrow) is only coincident with a TEC depletion, since the plasmapause has been eroded to lower L-shell and latitude.

4.2.2.1 Erosion on the plasmasphere

The double-peak feature in the WIDs is examined by Lin et al. (2021), who used the MAGE model to perform a set of controlled numerical experiments and demonstrated that the diffuse electron precipitation plays a crucial role in causing the latitudinal structure of the SAPS electric field. Figures 8(a) - (d) show the sampled FAC, electron precipitation, ionospheric conductance and electric field strength along 18 MLT at 07:07UT 03-31-2001. The green shade marks the auroral region which consists of the diffuse electron precipitation and the mono-energetic electron precipitation. The electron precipitation increases the local ionization rate in the ionosphere E-region and enhances the Pedersen and Hall conductance. A portion of the Region-2 current is located equatorward of the diffuse electron precipitation, where the conductance is comparatively low. This leads to a strong poleward electrostatic field in the sub-auroral region marked by the orange shade. The sub-auroral polarization stream (SAPS) is the WID that is constrained between the low latitude boundary of the dusk-side diffuse electron precipitation and the low latitude boundary of the dusk-side Region-2 current. The SAPS velocity peaks around 45°~50° and it overlaps with the plasmapause, causing a sunward ion flow shown in Figure 8(f). The advection flow transports the cold plasma away from the plasmasphere and to the dayside, which explains the erosion on the plasmapause marked by the purple box in Figure 5(b). The velocity peak located at higher latitudes around 57° is inside the range of the Region-1 current. It peaks in the region between the diffuse and the mono-energetic precipitation where the conductance is also comparatively low and the closure of Region-1 and the Region-2 currents results in a strong electric field. This electric field causes WID velocity peak and we call it the convection return flow (CRF). The CRF does not interact with the plasmasphere, which is consistent with Figure 5(b).

4.2.2.1 Depletion of the TEC

Figure 8(g) shows the MLAT profile of TEC, where there are two electron density/TEC troughs with one co-located with the peak of CRF around 55 MLAT and the other located around 42 MLAT, to the equatorward of the SAPS peak. The factors that contribute to the depletion of the ionospheric TEC are much more complicated than the plasmaspheric erosion. The formation of the electron density trough is discussed by Lu et al. (2020), where they examined the rate of change for O^+ density in the TIEGCM, which is considered as a proxy for the electron content. In general, the rate of change is determined by the O^+ production and loss rate, ambipolar diffusion, neutral wind transport, and the $\mathbf{E}\times\mathbf{B}$ transport. Lu et al. gave a detailed analysis of the contribution from each process. They showed that the $\mathbf{E}\times\mathbf{B}$ transport is the major contributor to the formation of the sub-auroral electron density trough. This transport brings the low electron density into the high-density region, and this depletion is further enhanced with the increased loss/recombination rate of the ions at a higher temperature caused by the significantly enhanced frictional heating due to the strong ion drifts in the WID channel (Schunk et al., 1976). The analysis above is consistent with our results. However, the equatorward shift of the midlatitude electron density trough in Figure 8(g) indicates other transport effects and needs further investigation in the future.

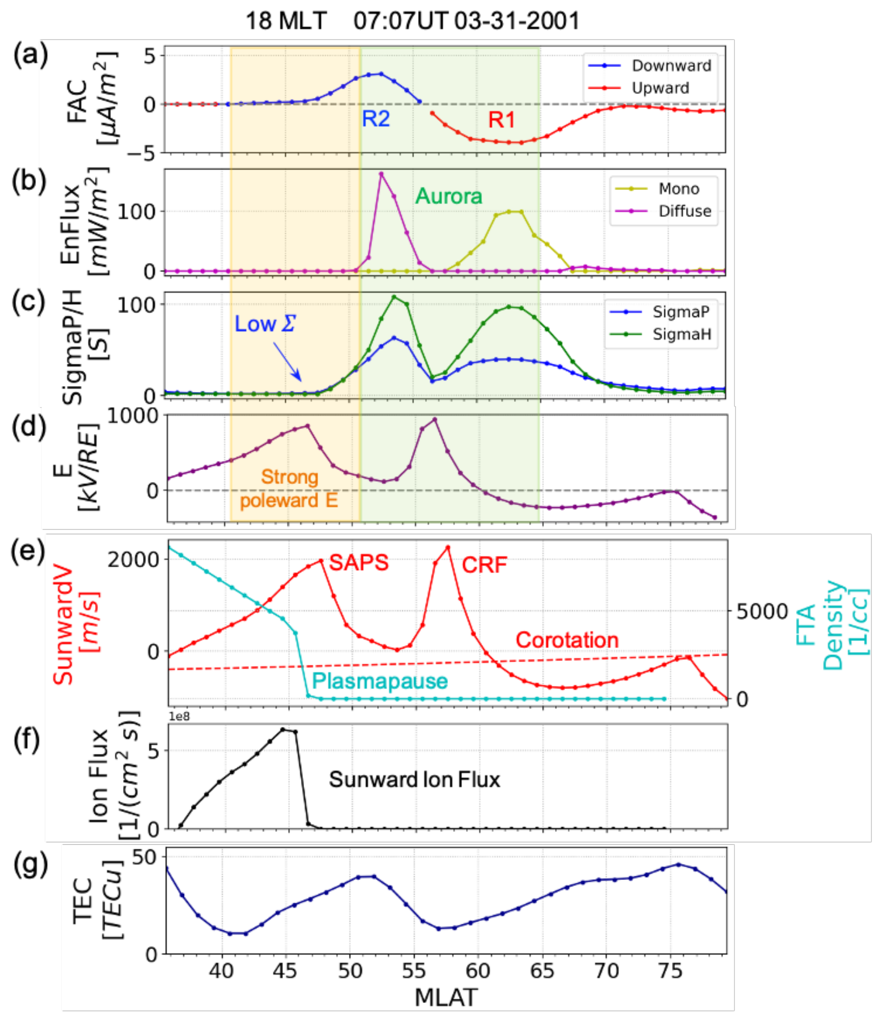

Figure 8. (a)-(e) Latitudinal profiles of REMIX ionospheric quantities sampled at 18 MLT and 07:07UT. **(a)** Upward Region-1(red) and downward Region-2 current (blue). **(b)** Energy flux of diffuse (magenta) and mono-energetic (olive) electron precipitation. **(c)** Pedersen conductance (blue) and Hall conductance (green). **(d)** Electric field strength. **(e)** Calculated E×B ion drift velocity (red) with corotation velocity shown by the dashed line. The cyan curve is the flux-tube-averaged (FTA) plasmaspheric density mapped to the ionospheric grid. **(f)** Calculated sunward ion flux based on density and ion drift velocity in **(e). (g)** Total electron content.

4.2.2.1 Data-model comparison on the erosion effect

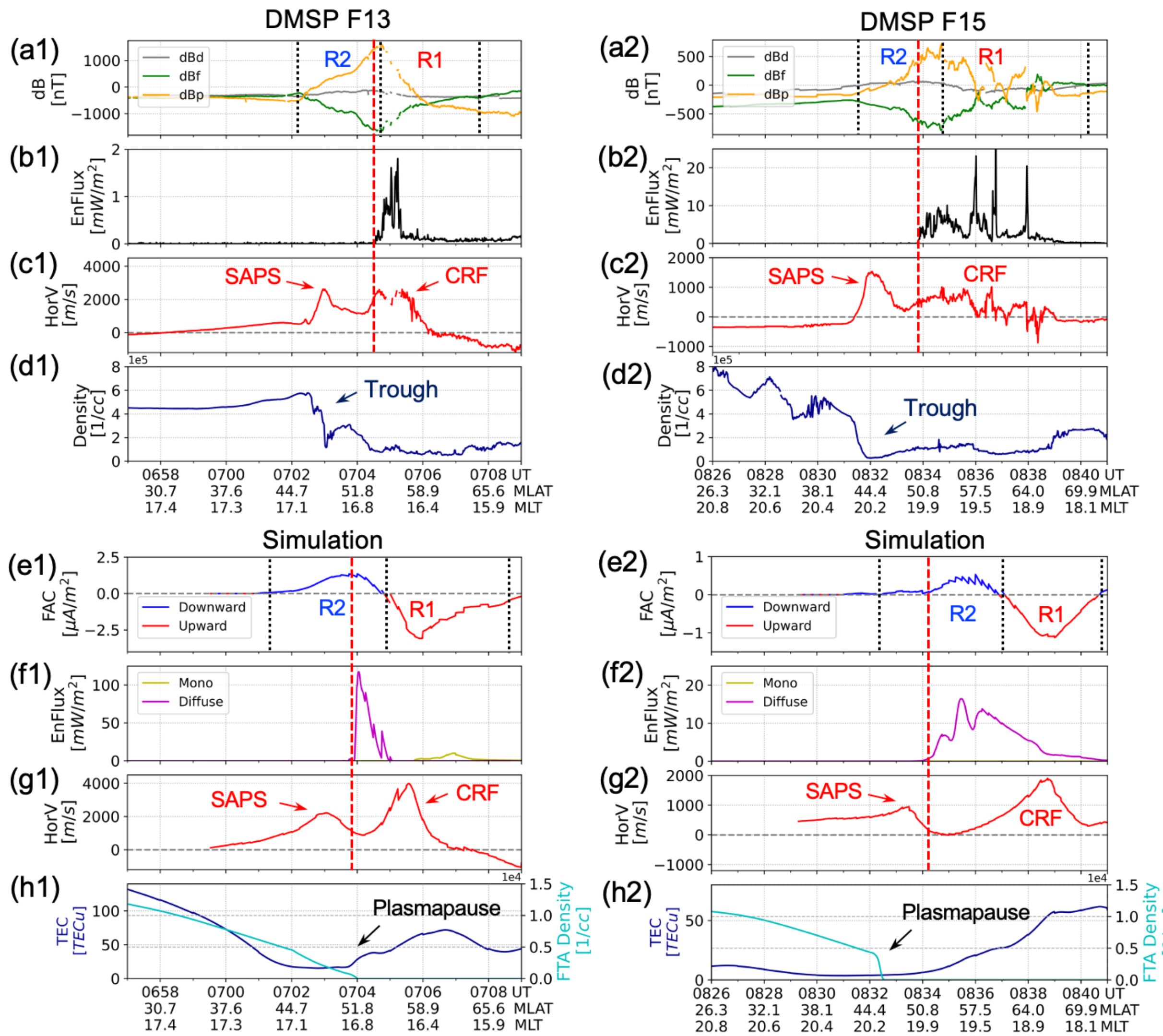

Figure 9. DMSP F13 and F15 (~850km in altitude) measurements at 06:57 ~ 07:09UT, March 31, 2001: **(a1)-(a2)** magnetic perturbation in the downward (dBd), forward (dBf) and perpendicular (horizontal cross-track) (dBp) direction relative to the satellite track direction; **(b1)-(b2)** precipitating electron energy flux; **(c1)-(c2)** horizontal cross-track sunward ion drift velocity; and **(d1)-(d2)** electron density. The dashed black lines in **(a1)-(a2)** divide the range of the Region-1 and the Region-2 currents based on the slopes of the magnetic perturbation curves. The dashed red line is the equatorward auroral boundary. Simulated quantities sampled along the satellite track: **(e1)-(e2)** field-aligned current; **(f1)-(f2)** energy flux of diffuse electron precipitation (magenta) and mono-energetic precipitation (olive); **(g1)-(g2)** simulated ion drift velocity in the DMSP horizontal cross-track sunward direction; **(h1)-(h2)** simulated electron density (navy) and flux-tube-averaged plasmaspheric density (black).

Sections 4.2.2.1 and 4.2.2.2 discuss the double-peak feature in WIDs on the dusk side and their effect on the plasmaspheric erosion and ionospheric TEC depletion. In this section, we investigate this subject with DMSP observations. Figure 9 shows a data-model comparison of the FAC, the ionospheric differential number flux of the electron precipitation, the horizontal ion drift velocity, and the electron density. Figures 9(a1) - (d1) and (a2) - (d2) are DMSP F13 and F15 measurements during 06:57 ~ 07:09UT and 08:26 ~ 08:41UT, 03-31-2001 respectively. Ranges of the Region-1 and the Region-2 currents can be derived from the magnetic field perturbation following the method from J. Liu et al. (2022), which are divided by the back dashed line in Figures 9(a1) and (a2). Figures 9(e1) - (h1) and (e2) - (h2) are the corresponding physical quantities from the MAGE simulation along the satellite trajectories. Since the satellites usually fly beyond the altitude range of TIEGCM, we plot the TEC and the plasmaspheric flux-tube-averaged (FTA) density instead. The dashed red line is the equatorward auroral boundary using the same criteria as in Figure 8.

Figures 9(a1) - (d1) and (a2) - (d2) show that dusk-side electron precipitation is located mostly within the range of the Region-1 current with a slight overlap on the Region-2 current. The SAPS is located in the sub-auroral region within the range of the Region-2 current. The CRF covers the region between the Region-1 and Region-2 current and some portion of the Region-1 current. The spikes in the electron precipitation, e.g., around 55 MLAT at 07:05UT correspond to the dips in the CRF velocity. The large velocity of SAPS (Figure 9(c1)) is collocated with an acute trough in the ionospheric electron density. The electron density is also low at higher latitudes, corresponding to the location of CRF. This is consistent with the result shown in Figure 8.

Compared with the DMSP data, the simulation predicts similar location of the Region-1/2 currents and electron precipitation. The model overestimates the strength of the precipitation energy flux in Figure 9(f1), but according to the following REMIX output it is transient and it does not impact the ionospheric conductance much. In terms of the WID velocity, the double-band feature of WIDs, SAPS and CRF peaks, are successfully reproduced. The SAPS velocity is around 2000 m/s at 07:03UT and 1000m/s at 08:33UT, which are in reasonable agreement with the observations.

In Figures 9(h1) and (h2), the location of the plasmapause and the TEC depletion can be seen and compared with the observations. The simulated TEC troughs corresponding to SAPS are much broader than the electron density troughs in the observation. The FTA plasmaspheric density, on the other hand, has good agreement with the observations of the electron density in Figures 9(d1) and (d2): At 07:03UT (near 48 MLAT,17 MLT), in the observation (Figure 9(d1)), the SAPS velocity peak still overlaps with the region with substantial electron content and causing a density trough to mirror the SAPS peak. In the simulation (Figure 9(h1)), the SAPS peak also overlaps with a portion of the plasmasphere which causes sunward plasmaspheric particle transport. In the later satellite pass at 08:32UT (near 46 MLAT, 20 MLT) as shown in Figure 9(d2), the SAPS velocity peak corresponds to a substantially depleted electron density that forms a distinct boundary in the density profile. In the simulation (Figure 9(h2)), the same sharp drop in the FTA density is captured by the model. Combined with the analysis of the sunward ion flux caused by SAPS at the plasmapause in Figure 8(e)-(f), this data-model comparison confirms the effect of SAPS in depleting the local plasma content.

In Section 4.2, we have discussed the formation of the WIDs and investigated their role in depleting the local plasma density. During storm main phase, in both simulation and observation, two velocity peaks can be found in the WIDs. The one at the midlatitude is the SAPS channel. The transportation effect of SAPS causes the erosion of the plasmapause at its dusk side and the TEC depletion in the trough region. In the next section, we further investigate the factors that determine the spatial distribution of Region-2 current and the electron precipitation that lead to the SAPS electric field and their relation to the geospace plume evolution.

4.3 Relationship between ring current build-up and geospace plume development

As discussed in Section 4.2, the Region-2 current and electron precipitation directly control the SAPS electric field development in the ionosphere. In this section, we further explore the major factors in the magnetosphere that drive SAPS development and the geospace plume evolution from the perspective of M-I coupling.

Figures 10(a) and Figure11(a) show contours of the specified values in the plasma profile as a marker of the plasmapause (black), the ring current ion pressure (red), the electron pressure (green), the equatorial mapping of the energy flux of diffuse electron precipitation (orange), the FAC (background) and the electrostatic potential (light solid and dashed contours) at the beginning (04:48UT) and the end (07:41UT) of the storm main phase. The variable values enclosed by the colored contour lines are larger than the contour values. The contour values are chosen to best describe the spatial distribution of the variables (see Figure S1). The red arrows point to the critical region, where the dusk-side Region-2 current (in blue) is located. At the sunward azimuthal edge of the ring current ion pressure (represented by the magenta contour), the large pressure gradient distorts the magnetic field lines and generates the Region-2 current that connects to the partial ring current and flows into the ionosphere. The magnetospheric source region of diffuse precipitation is located in the region with high electron pressure and it partially overlaps with the Region-2 current. This results in a strong SAPS electric field co-located with the low-latitude portion of the Region-2 current where there is little electron precipitation. This result is consistent with previous MAGE modeling work of SAPS (Lin et al., 2021) and earlier works describing the basic physics of SAPS (e.g., Foster & Vo, 2002).

During the period of geospace plume erosion by SAPS (from Figure 11(a) to Figure 11(a)), the high electron pressure region, which is the source region of the electron precipitation, is always located at the outer boundary of the ring current ion pressure 100 nPa contour. As a result, the electron precipitation always covers a portion of the Region-2 current which maintains the persistent SAPS electric field located at the inner boundary of the ring current contour and the dusk edge of the plasmapause. The strong SAPS electric field dominates the spatial distribution of the electric potential and evolves the plasmaspheric plume into the dusk side. The joint evolution of the ring current and the plasmasphere is shown in Movie S3 and a similar spatial relation of the two is observed by the IMAGE satellite (Figure S2).

We now ask, what determines the spatial distributions of the ring current electron and ion pressure that impact the source regions of diffuse electron precipitation and the Region-2 currents? The cold plasmaspheric protons are subject to the $\mathbf{E}\times\mathbf{B}$ drift and corotation. Besides these two drifts, the hot protons and electrons, after being transported to the inner magnetosphere, are also subjected to gradient/curvature drift in opposite directions. In RCM, the total drift effect is represented by the effective potential defined by adding the term $V^{-2/3} \cdot \lambda_{i,k}/e$ to the equatorial electric potential (Toffoletto et al., 2003). This effective electric potential for species *i* at energy channel *k* is given by

$$\phi_{eff,k,i} = \phi_I + \lambda_{i,k} \cdot V^{-\frac{2}{3}}/e + \phi_c \quad (3)$$

where $\lambda_{i,k}$ is the energy invariant for species *i* at channel *k* in RCM and the closed magnetic flux tube volume *V* is given by

$$V = \int \frac{ds}{B_{MHD}} \quad (4)$$

Figures 10, 11(b) - (d) show the flux tube content (η) in the magnetic flux tube from the RCM characteristic energy channels of the plasmasphere ($\lambda_0 = 0$), hot protons and hot electrons at the beginning and the end of the storm main phase. The proton and the electron channels shown (λ_p= 1639.46, λ_e =-234.21, in RCM units, $eV \cdot (R_E/nT)^{\frac{2}{3}}$) are the ones that contribute most to the total proton pressure and the total electron pressure (as well as the diffuse precipitation energy flux) respectively. The corresponding energy of the proton and the electron at the selected channels is around 80 keV and 8 keV at the location of the ring current and the electron precipitation. The effective potential of the channel is plotted as black contour lines with dashed lines for negative values.

Comparing the effective electric potential contours in Figures 10 (b) - (d), we can see the gradient and curvature term in the proton effective electric field ($Potential\_P$) dominates the inner magnetosphere and is a result of the comparatively large energy invariant of that proton channel. The electron effective electric potential ($Potential\_E$) contours look similar to the plasmaspheric electric potential ($Potential\_0$)) especially outside the geosynchronous orbit, since the gradient and curvature term for electrons is comparatively weak due to their lower particle energy. During the early main phase, the ring current particles have just been transported by the convection electric field to the inner magnetosphere and started to drift following their effective electric potential contours. Meanwhile, the plasmaspheric plume expands sunward driven by the convection electric field. At this moment, the η distributions of the plasmasphere, proton and electron are approximately symmetric about the x-axis (Y = 0) and the conditions for the SAPS formation have just started to appear on the dusk edge of the plasmasphere.

At the late main phase, as shown in Figure 11(c), the η distribution shows that the ring current hot protons have drifted westward from the nightside and penetrated deep inside $2R_E$ on the dayside (marked by the yellow arrow). The Region-2 current originating at the outer edge of the partial ring current beyond $2R_E$ has shifted toward the dayside accordingly (in Figure 11(a)). The SAPS electric field have been very strong and dominated the geometry of Potential_0 and Potential_E. On one hand, it causes the plamaspheric plume to move to the dusk side. On the other hand, the hot electrons (in Figure 11(d)) are obstructed by the strong dusk-side electric fields with major contribution from SAPS. The electrons accumulate outside the SAPS flow channel around $3R_E$ and form a sharp edge in the electron η distribution (marked by the orange arrow). This leads to a distinct equatorward edge of the ionospheric diffuse precipitation and the absence of electron precipitation in part of the Region-2 current that helps to maintain the strong SAPS electric field.

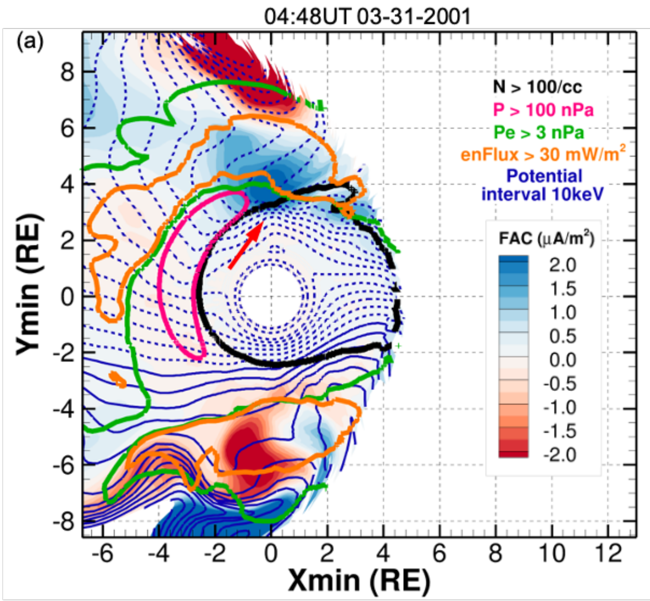

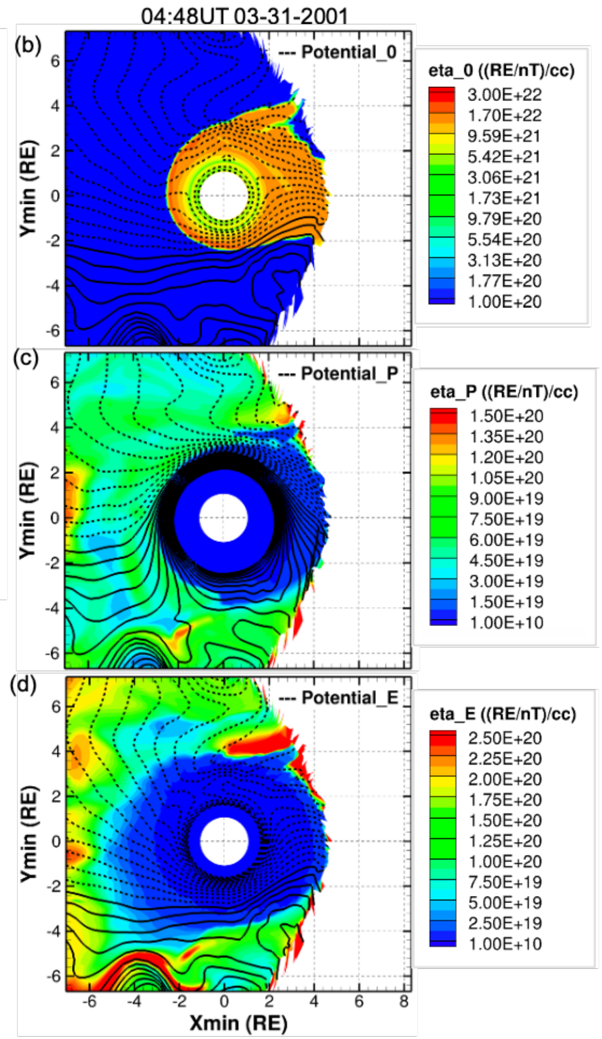

Figure 10. (a) Contour plots of the equatorial plane view of plasmapause (black), ring current pressure (pink), electron pressure (green), equatorial energy flux of diffuse electron precipitation (orange), electrostatic potential with 10kV spacing (navy, dashed for negative values) and FAC (red-blue) on the equatorial plane at the early main phase. The red arrow points to the location where the Region-2 current is strong while the diffuse precipitation is weak and the resultant (SAPS) electrostatic field is intense. **(b)-(d)** Contour plots of the RCM η variable for the plasmaspheric energy channel, the proton energy channel that contributes most to the ring current pressure and the electron energy channel that contributes most to the electron pressure/diffuse precipitation energy flux and their corresponding effective electric potential on the equatorial plane.

The analysis above demonstrates that the storm-time energy-dependent electron and proton drifts determine the spatial distribution of Region-2 currents and diffuse electron precipitation. The ring current ion can overcome the existing SAPS electric field and penetrate into deeper L-shell at dayside, while the ring current electrons cannot due to their featured adiabatic invariants of their drifts. This delicate balance between the energy-dependent gradient/curvature drift and the **E**×**B** drifts self-consistently maintains the SAPS electric field to further erode the dusk-side plasmasphere and push the plasmaspheric plume shifting toward the dusk side.

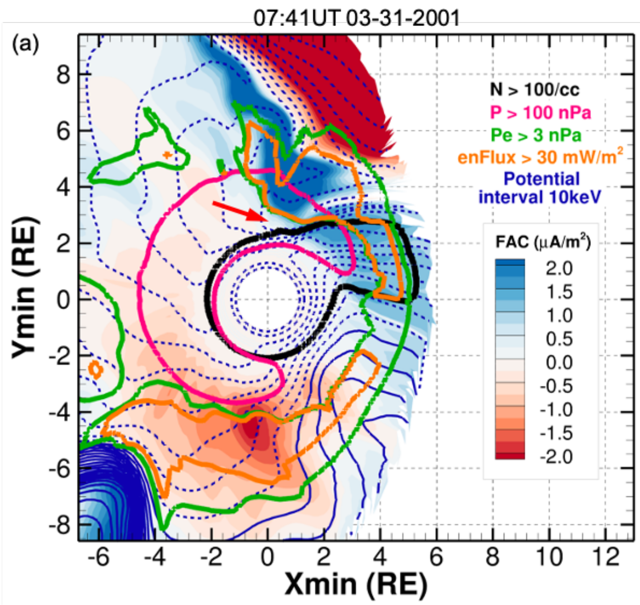

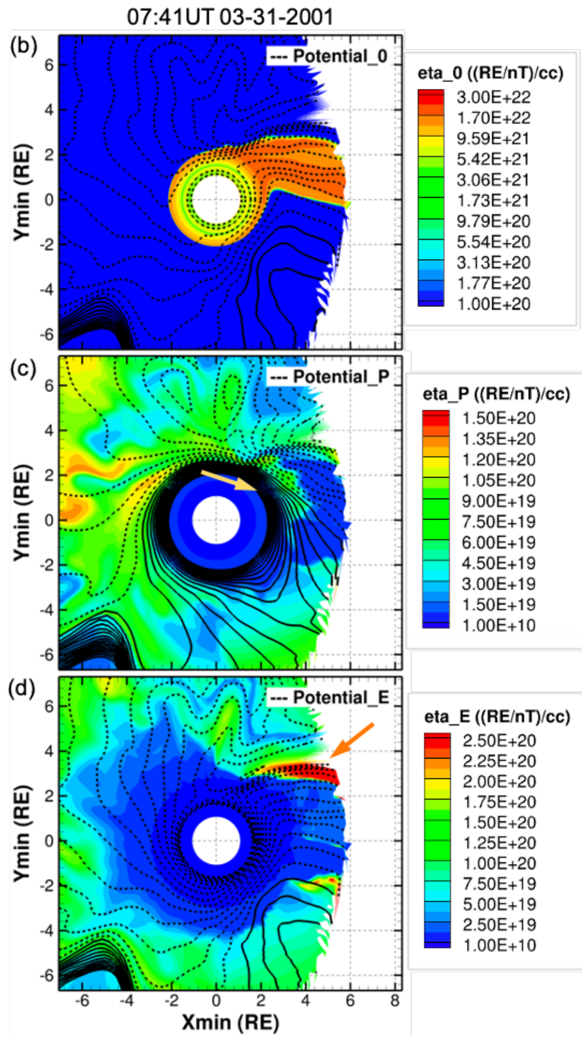

Figure 11. Same variables as in Figure 10. At the late main phase, the dawn-dusk asymmetry in the plasmaspheric plume has developed as a result of the dominant SAPS electric field on its dusk side.

4.5 Model limitations

The MAGE simulation of the March 31, 2001 storm presented above demonstrates clearly the close relation between the global-scale convection, ring current build-up, FAC, and electron precipitation which dynamically alter the geospace plume system. However, there are some limitations. First, the model did not include the plasma transport between the plasmasphere and the ionosphere. Although, as discussed in Section 1.2.2.2, plasmaspheric refilling is much slower compared with the dynamic transport of the plasma within the plasmasphere and ionosphere during the storm main phase (Lawrence et al., 1999; Denton et al., 2012; Krall et al., 2014), plasma exchange between the plasmasphere and ionosphere can be important in the storm recovery phase (Carpenter & Lemaire, 1997). Second, as discussed in Section 4.3, during the later stage of the storm main phase, the simulated ring current overlaps with the plasmasphere, especially in the plume region. In this work, our model did not include ring current ion loss due to the EMIC wave scattering (Erlandson & Ukhorskiy, 2001; Goldstein et al., 2003), although it is possible that ion precipitation may affect the ionospheric conductance and feed back to the magnetospheric system (Tian et al., 2022). Furthermore, inside the plasmasphere, the energetic electrons resonate with hiss waves and contribute to diffuse electron precipitation (Ma et al., 2021). The current version of the model did not take into account such wave-particle interactions. We are working on including these important precipitation mechanisms to better inform the ring current particle loss and ionospheric precipitation in future versions of the model (Bao et al., 2022; Lin et al., 2022).

4 Summary and Conclusions

In this paper, we investigate the evolution of the geospace plume during the March 31, 2001 superstorm using the MAGE model, which coupled the global and inner magnetosphere, the ionosphere and the thermosphere. Combined with satellite observations, we used the MAGE simulation to address the three major science questions raised in the introduction section.

The first question is the cause of the linkage and joint evolution of the two counterparts of the geospace plume, the plasmaspheric plume and the ionospheric SED plume. We conclude that the **E**×**B** transport of the plasma by the coupled magnetosphere-ionosphere electric field is the major process that causes the plasmaspheric plume and the ionospheric SED plume to evolve in a similar way and to have co-located footprints on the equatorial plane.

The second and third science questions are closely tied together. The second science question focuses on identifying the specific processes that are important for shaping the plasmasphere and the ionosphere plume. The third science question explores the relationship between the build-up of the ring current and the development of the geospace plume. The simulation shows that geospace plume in the equatorial plane expands sunward due to the convection electric field in the early main phase. The plume shifts toward the dusk side in the late main phase. We also find two channels of TEC depletion, with one in the ionosphere midlatitude trough region, corresponding to the dusk edge of the plasmasphere, and the other at higher latitudes inside the auroral oval. By investigating the related physical quantities along 18 MLT and comparing with DMSP observations, we find that the westward SAPS flow is the major cause of the erosion on the dusk edge of the plasmasphere and duskward shift of the geospace plume, which answers science question two. We further investigate the cause of the spatial distributions of the Region-2 currents and diffuse precipitation that are responsible for the occurrence of SAPS by analyzing the effective electric fields of ring current protons and electrons. Region-2 current is located at the sunward boundary of the ring current mostly contributed by hot protons, where the pressure gradient distorts the magnetic field. Due to the energy-dependent charged particle drifts, the ring current pressure is located preferentially on the dusk side. The region of energetic ring current electrons, as the source region of the diffuse precipitation, are at larger L-shells compared to the region of high ion pressure. As a result, the SAPS electric field is generated at the location where a part of the Region-2 current does not overlap with the diffuse precipitation and the ionospheric conductance is low. The analysis of the RCM energy channels shows the ring current ions can overcome the existing SAPS electric field and penetrate into deeper L-shell at dayside, while the ring current electrons cannot due to their featured adiabatic invariants of their drifts. This delicate balance between the energy-dependent gradient/curvature drift and the **E**×**B** drifts self-consistently maintains the SAPS electric field. We conclude that the intrinsic cause of the SAPS and the resulting plasmasphere erosion as well as the plume geometry is the energy-dependent drifts of the ring current electrons and ions that impact the coupled geospace system.

Acknowledgments

This work is supported by NASA DRIVE Science Center for Geospace Storms (CGS) grant 80NSSC22M0163, NASA O2R grant 80NSSC19K0241, NASA GCR grant 80NSSC17K0013 and LWS grant 80NSSC20K0356. Dr. Viacheslav Merkin gratefully acknowledges support from NASA LWS grants 80NSSC19K0080 and 80NSSC19K0071. We would like to acknowledge the use of computational resources (doi:10.5065/D6RX99HX) at the NCAR-Wyoming Supercomputing Center provided by the National Science Foundation and the State of Wyoming, and supported by NCAR's Computational and Information Systems Laboratory. Dr. Shanshan Bao thanks Dr. Joe Huba and Dr. Roger Varney for the valuable discussion on the modeling work. The OMNI data are obtained from https://cdaweb.gsfc.nasa.gov/index.html/; the World-wide TEC data and the DMSP data are provided by the CEDAR Madrigal Database (http://cedar.openmadrigal.org/index.html); the simulation data selected for figures in this paper are stored and published on Zenodo (via: https://zenodo.org/record/7843840).

References

Bao, S. (2019). Large-scale Coupled Models of the Inner Magnetosphere. Diss., Rice University. Retrieved from https://hdl.handle.net/1911/107801.

Bao, S., Toffoletto, F., Yang, J., Sazykin, S., & Wiltberger, M. (2021). Coupling the Rice Convection Model-Equilibrium to the Lyon-Fedder-Mobarry Global Magnetohydrodynamic Model. *Journal of Geophysical Research: Space Physics*, *126*(8). https://doi.org/10.1029/2020JA028973

Bao, S., Lin, D., Sorathia, K., Wang, D., Toffoletto, F., Merkin, V., et al. (2022). Wave-dependent ring current electron loss and magnetospheric precipitation during a geospace storm. *AGU Fall Meeting Abstracts*, *2022*, SM22F-1988.

Burch, J. L., Mitchell, D. G., Sandel, B. R., Brandt, P. C., & Wüest, M. (2001). Global dynamics of the plasmasphere and ring current during magnetic storms. *Geophysical Research Letters*, *28*(6), 1159–1162. https://doi.org/10.1029/2000GL012413

Carpenter, D. L., & Lemaire, J. (1997). Erosion and recovery of the plasmasphere in the plasmapause region. *Space Science Reviews*, *80*(1/2), 153–179. https://doi.org/10.1023/A:1004981919827

Cramer, W. D., Raeder, J., Toffoletto, F. R., Gilson, M., & Hu, B. (2017). Plasma sheet injections into the inner magnetosphere: Two-way coupled OpenGGCM-RCM model results. *Journal of Geophysical Research: Space Physics*, *122*(5), 5077–5091. https://doi.org/10.1002/2017JA024104

De Zeeuw, D. L., Sazykin, S., Wolf, R., Gombosi, T., Ridley, A., & Toth. (2004). Coupling of a global MHD code and an inner magnetospheric model: Initial results. *Journal of Geophysical Research*, *109*(A12), A12219. https://doi.org/10.1029/2003JA010366

Denton, R. E., Wang, Y., Webb, P. A., Tengdin, P. M., Goldstein, J., Redfern, J. A., & Reinisch, B. W. (2012). Magnetospheric electron density long-term (>1 day) refilling rates inferred from passive radio emissions measured by IMAGE RPI during geomagnetically quiet times: MAGNETOSPHERIC ELECTRON DENSITY REFILLING RATES. *Journal of Geophysical Research: Space Physics*, *117*(A3), n/a-n/a. https://doi.org/10.1029/2011JA017274

Erlandson, R. E., & Ukhorskiy, A. J. (2001). Observations of electromagnetic ion cyclotron waves during geomagnetic storms: Wave occurrence and pitch angle scattering. *Journal of Geophysical Research: Space Physics*, *106*(A3), 3883–3895. https://doi.org/10.1029/2000JA000083

Fagundes, P. R., Cardoso, F. A., Fejer, B. G., Venkatesh, K., Ribeiro, B. A. G., & Pillat, V. G. (2016). Positive and negative GPS-TEC ionospheric storm effects during the extreme space weather event of March 2015 over the Brazilian sector: POSITIVE AND

NEGATIVE IONOSPHERIC STORM. *Journal of Geophysical Research: Space Physics*, *121*(6), 5613–5625. https://doi.org/10.1002/2015JA022214

Foster, J. C., & Burke, W. J. (2002). SAPS: A new categorization for sub-auroral electric fields. *Eos, Transactions American Geophysical Union*, *83*(36), 393. https://doi.org/10.1029/2002EO000289

Foster, J. C., & Vo, H. B. (2002). Average characteristics and activity dependence of the subauroral polarization stream: SUBAURORAL POLARIZATION STREAM. *Journal of Geophysical Research: Space Physics*, *107*(A12), SIA 16-1-SIA 16-10. https://doi.org/10.1029/2002JA009409

Foster, J. C., Erickson, P. J., Coster, A. J., Goldstein, J., & Rich, F. J. (2002). Ionospheric signatures of plasmaspheric tails. *Geophysical Research Letters*, *29*(13), 1623. https://doi.org/10.1029/2002GL015067

Foster, J. C., Erickson, P. J., Coster, A. J., Thaller, S., Tao, J., Wygant, J. R., & Bonnell, J. W. (2014). Storm time observations of plasmasphere erosion flux in the magnetosphere and ionosphere: Foster et al.: Plasmasphere Erosion Flux. *Geophysical Research Letters*, *41*(3), 762–768. https://doi.org/10.1002/2013GL059124

Foster, J. C., Erickson, P. J., Walsh, B. M., Wygant, J. R., Coster, A. J., & Zhang, Q. (2020). Multi-Point Observations of the Geospace Plume. In Q. Zong, P. Escoubet, D. Sibeck, G. Le, & H. Zhang (Eds.), *Geophysical Monograph Series* (1st ed., pp. 243–264). Wiley. https://doi.org/10.1002/9781119509592.ch14

Foster, J.C., Rideout, W., Sandel, B., Forrester, W. T., & Rich, F. J. (2007). On the relationship of SAPS to storm-enhanced density. *Journal of Atmospheric and Solar-Terrestrial Physics*, *69*(3), 303–313. https://doi.org/10.1016/j.jastp.2006.07.021

Foster, John C. (1993). Storm time plasma transport at middle and high latitudes. *Journal of Geophysical Research: Space Physics*, *98*(A2), 1675–1689. https://doi.org/10.1029/92JA02032

Gallagher, D. L., Craven, P. D., & Comfort, R. H. (2000). Global core plasma model. *Journal of Geophysical Research: Space Physics*, *105*(A8), 18819–18833. https://doi.org/10.1029/1999JA000241

Goldstein, J. (2004). Simultaneous remote sensing and in situ observations of plasmaspheric drainage plumes. *Journal of Geophysical Research*, *109*(A3), A03202. https://doi.org/10.1029/2003JA010281

Goldstein, J. (2007). Plasmasphere Response: Tutorial and Review of Recent Imaging Results. *Space Science Reviews*, *124*(1–4), 203–216. https://doi.org/10.1007/s11214-006-9105-y

Goldstein, J., & Sandel, B. R. (2005). The global pattern of evolution of plasmaspheric drainage plumes. In J. Burch, M. Schulz, & H. Spence (Eds.), *Geophysical Monograph Series* (Vol. 159, pp. 1–22). Washington, D. C.: American Geophysical Union. https://doi.org/10.1029/159GM02

Goldstein, J., Sandel, B. R., Hairston, M. R., & Reiff, P. H. (2003). Control of plasmaspheric dynamics by both convection and sub-auroral polarization stream: PLASMASPHERIC DYNAMICS. *Geophysical Research Letters*, *30*(24). https://doi.org/10.1029/2003GL018390

Goldstein, J., Burch, J. L., & Sandel, B. R. (2005). Magnetospheric model of subauroral polarization stream: MAGNETOSPHERIC SAPS MODEL. *Journal of Geophysical Research: Space Physics*, *110*(A9). https://doi.org/10.1029/2005JA011135

Goldstein, J., Thomsen, M. F., & DeJong, A. (2014). In situ signatures of residual plasmaspheric plumes: Observations and simulation. *Journal of Geophysical Research: Space Physics*, *119*(6), 4706–4722. https://doi.org/10.1002/2014JA019953

Huba, J., & Krall, J. (2013). Modeling the plasmasphere with SAMI3: MODELING THE PLASMASPHERE WITH SAMI3. *Geophysical Research Letters*, *40*(1), 6–10. https://doi.org/10.1029/2012GL054300

Huba, J. D., & Sazykin, S. (2014). Storm time ionosphere and plasmasphere structuring: SAMI3-RCM simulation of the 31 March 2001 geomagnetic storm. *Geophysical Research Letters*, *41*(23), 8208–8214. https://doi.org/10.1002/2014GL062110

Huba, J. D., Sazykin, S., & Coster, A. (2017). SAMI3-RCM simulation of the 17 March 2015 geomagnetic storm. *Journal of Geophysical Research: Space Physics*, *122*(1), 1246–1257. https://doi.org/10.1002/2016JA023341

Krall, J., Huba, J. D., Denton, R. E., Crowley, G., & Wu, T.-W. (2014). The effect of the thermosphere on quiet time plasmasphere morphology. *Journal of Geophysical Research: Space Physics*, *119*(6), 5032–5048. https://doi.org/10.1002/2014JA019850

Lawrence, D. J., Thomsen, M. F., Borovsky, J. E., & McComas, D. J. (1999). Measurements of early and late time plasmasphere refilling as observed from geosynchronous orbit. *Journal of Geophysical Research: Space Physics*, *104*(A7), 14691–14704. https://doi.org/10.1029/1998JA900087

Lemaire, J. F., Gringauz, K. I., Carpenter, D. L., & Bassolo, V. (1998). *The Earth's Plasmasphere* (1st ed.). Cambridge University Press. https://doi.org/10.1017/CBO9780511600098

Lin, C. H., Richmond, A. D., Heelis, R. A., Bailey, G. J., Lu, G., Liu, J. Y., et al. (2005). Theoretical study of the low- and midlatitude ionospheric electron density enhancement during the October 2003 superstorm: Relative importance of the neutral wind and the electric field. *Journal of Geophysical Research*, *110*(A12), A12312. https://doi.org/10.1029/2005JA011304

Lin, D., Wang, W., Scales, W. A., Pham, K., Liu, J., Zhang, B., et al. (2019). SAPS in the 17 March 2013 Storm Event: Initial Results From the Coupled Magnetosphere-Ionosphere-Thermosphere Model. *Journal of Geophysical Research: Space Physics*, *124*(7), 6212–6225. https://doi.org/10.1029/2019JA026698

Lin, D., Sorathia, K., Wang, W., Merkin, V., Bao, S., Pham, K., et al. (2021). The role of diffuse electron precipitation in the formation of subauroral polarization streams. *Journal of Geophysical Research: Space Physics*. https://doi.org/10.1029/2021JA029792

Lin, D., Wang, W., Merkin, V., Bao, S., Sorathia, K., Pham, K., et al. (2022). Characterizing auroral precipitation and ionospheric conductance with the Multiscale Atmosphere-Geospace Environment model. *AGU Fall Meeting Abstracts*, *2022*, SA24A-01.

Lin, D., Wang, W., Merkin, V. G., Huang, C., Oppenheim, M., Sorathia, K., et al. (2022). Origin of Dawnside Subauroral Polarization Streams During Major Geomagnetic Storms. *AGU Advances*, *3*(4). https://doi.org/10.1029/2022AV000708

Liu, J., Higuchi, T., Lyons, L. R., Ohtani, S., Wu, J., Zou, Y., et al. (2022). The Occurrence of Embedded Region 1 and 2 Currents Depends on Geomagnetic Activity Level. *Journal of Geophysical Research: Space Physics*, *127*(11). https://doi.org/10.1029/2022JA030539

Liu, Jing, Wang, W., Burns, A., Yue, X., Zhang, S., Zhang, Y., & Huang, C. (2016). Profiles of ionospheric storm-enhanced density during the 17 March 2015 great storm. *Journal of*

Geophysical Research: Space Physics, *121*(1), 727–744. https://doi.org/10.1002/2015JA021832

Lu, G., Zakharenkova, I., Cherniak, I., & Dang, T. (2020). Large-Scale Ionospheric Disturbances During the 17 March 2015 Storm: A Model-Data Comparative Study. *Journal of Geophysical Research: Space Physics*, *125*(5). https://doi.org/10.1029/2019JA027726

Ma, Q., Li, W., Zhang, X. -J., Bortnik, J., Shen, X. -C., Connor, H. K., et al. (2021). Global Survey of Electron Precipitation due to Hiss Waves in the Earth's Plasmasphere and Plumes. *Journal of Geophysical Research: Space Physics*, *126*(8). https://doi.org/10.1029/2021JA029644

Merkin, V. G., & Lyon, J. G. (2010). Effects of the low-latitude ionospheric boundary condition on the global magnetosphere: IONOSPHERE/MAGNETOSPHERE GLOBAL EFFECTS. *Journal of Geophysical Research: Space Physics*, *115*(A10), n/a-n/a. https://doi.org/10.1029/2010JA015461

Moldwin, M. B., Zou, S., & Heine, T. (2016). The story of plumes: the development of a new conceptual framework for understanding magnetosphere and ionosphere coupling. *Annales Geophysicae*, *34*(12), 1243–1253. https://doi.org/10.5194/angeo-34-1243-2016

Pembroke, A., Toffoletto, F., Sazykin, S., Wiltberger, M., Lyon, J., Merkin, V., & Schmitt, P. (2012). Initial results from a dynamic coupled magnetosphere-ionosphere-ring current model. *Journal of Geophysical Research: Space Physics*, *117*(A2), 2011JA016979. https://doi.org/10.1029/2011JA016979

Pham, K. H., Zhang, B., Sorathia, K., Dang, T., Wang, W., Merkin, V., et al. (2022). Thermospheric Density Perturbations Produced by Traveling Atmospheric Disturbances

During August 2005 Storm. *Journal of Geophysical Research: Space Physics*, *127*(2). https://doi.org/10.1029/2021JA030071

Pulkkinen, T. I., Tsyganenko, N. A., & Friedel, R. H. W. (Eds.). (2005). *The Inner Magnetosphere: Physics and Modeling* (Vol. 155). Washington, D. C.: American Geophysical Union. https://doi.org/10.1029/GM155

Qian, L., Burns, A. G., Emery, B. A., Foster, B., Lu, G., Maute, A., et al. (2014). The NCAR TIE-GCM: A Community Model of the Coupled Thermosphere/Ionosphere System. In Joseph Huba, R. Schunk, & G. Khazanov (Eds.), *Geophysical Monograph Series* (pp. 73–83). Chichester, UK: John Wiley & Sons, Ltd. https://doi.org/10.1002/9781118704417.ch7

Raeder, J., Cramer, W. D., Jensen, J., Fuller-Rowell, T., Maruyama, N., Toffoletto, F., & Vo, H. (2016). Sub-Auroral Polarization Streams: A complex interaction between the magnetosphere, ionosphere, and thermosphere. *Journal of Physics: Conference Series*, *767*, 012021. https://doi.org/10.1088/1742-6596/767/1/012021

Richmond, A. D., Ridley, E. C., & Roble, R. G. (1992). A thermosphere/ionosphere general circulation model with coupled electrodynamics. *Geophysical Research Letters*, *19*(6), 601–604. https://doi.org/10.1029/92GL00401

Sandel, B. R., King, R. A., Forrester, W. T., Gallagher, D. L., Broadfoot, A. L., & Curtis, C. C. (2001). Initial results from the IMAGE Extreme Ultraviolet Imager. *Geophysical Research Letters*, *28*(8), 1439–1442. https://doi.org/10.1029/2001GL012885

Schunk, R. W., Banks, P. M., & Raitt, W. J. (1976). Effects of electric fields and other processes upon the nighttime high-latitude *F* layer. *Journal of Geophysical Research*, *81*(19), 3271–3282. https://doi.org/10.1029/JA081i019p03271

Tian, X., Yu, Y., Zhu, M., Ma, L., Cao, J., Pr, S., et al. (2022). Effects of EMIC Wave-Driven Proton Precipitation on the Ionosphere. *Journal of Geophysical Research: Space Physics*, *127*(2). https://doi.org/10.1029/2021JA030101

Toffoletto, F., Sazykin, S., Spiro, R., & Wolf, R. (2003). Inner magnetospheric mod- eling with the rice convection model. *Space Science Reviews*, *107*(1/2), 175–196. https://doi.org/10.1023/A:1025532008047

Wang, W., Talaat, E. R., Burns, A. G., Emery, B., Hsieh, S., Lei, J., & Xu, J. (2012). Thermosphere and ionosphere response to subauroral polarization streams (SAPS): Model simulations: THE EFFECT OF SAPS ON THE T-I SYSTEM. *Journal of Geophysical Research: Space Physics*, *117*(A7), n/a-n/a. https://doi.org/10.1029/2012JA017656

Wolf, R. A. (1983). The Quasi-Static (Slow-Flow) Region of the Magnetosphere. In R. L. Carovillano & J. M. Forbes (Eds.), *Solar-Terrestrial Physics* (Vol. 104, pp. 303–368). Dordrecht: Springer Netherlands. https://doi.org/10.1007/978-94-009-7194-3_14

Zhang, B., Lotko, W., Brambles, O., Wiltberger, M., & Lyon, J. (2015). Electron precipitation models in global magnetosphere simulations. *Journal of Geophysical Research: Space Physics*, *120*(2), 1035–1056. https://doi.org/10.1002/2014JA020615

Zhang, Binzheng, Sorathia, K. A., Lyon, J. G., Merkin, V. G., Garretson, J. S., & Wiltberger, M. (2019). GAMERA: A Three-dimensional Finite-volume MHD Solver for Non-orthogonal Curvilinear Geometries. *The Astrophysical Journal Supplement Series*, *244*(1), 20. https://doi.org/10.3847/1538-4365/ab3a4c

Zou, S., Ridley, A. J., Moldwin, M. B., Nicolls, M. J., Coster, A. J., Thomas, E. G., & Ruohoniemi, J. M. (2013). Multi-instrument observations of SED during 24-25 October

2011 storm: Implications for SED formation processes: SED FORMATION PROCESSES. *Journal of Geophysical Research: Space Physics*, *118*(12), 7798–7809. https://doi.org/10.1002/2013JA018860

Zou, S., Moldwin, M. B., Ridley, A. J., Nicolls, M. J., Coster, A. J., Thomas, E. G., & Ruohoniemi, J. M. (2014). On the generation/decay of the storm-enhanced density plumes: Role of the convection flow and field-aligned ion flow: Generation and Decay of SED Plumes. *Journal of Geophysical Research: Space Physics*, *119*(10), 8543–8559. https://doi.org/10.1002/2014JA020408

Zou, Y., Walsh, B. M., Shi, X., Lyons, L., Liu, J., Angelopoulos, V., et al. (2021). Geospace Plume and Its Impact on Dayside Magnetopause Reconnection Rate. *Journal of Geophysical Research: Space Physics*, *126*(6). https://doi.org/10.1029/2021JA029117

Journal of Geophysical Research: Space Physics

Supporting Information for

The relation among the ring current, subauroral polarization stream, and the geospace plume: MAGE Simulation of the March 31 2001 Super Storm

Shanshan Bao[1], Wenbin Wang[2], Kareem Sorathia[3], Slava Merkin[3], Frank Toffoletto[1], Dong Lin[2], Kevin Pham[2], Jeffrey Garretson[3], Michael Wiltberger[2], John Lyon[4] and Adam Michael[3]

[1]Department of Physics and Astronomy, Rice University, Houston TX

[2]High Altitude Observatory, National Center for Atmospheric Research, Boulder CO

[3]Applied Physics Laboratory, Johns Hopkins University, Laurel MD

[4]Department of Physics and Astronomy, Dartmouth College, Hanover NH

Corresponding author: Shanshan Bao (shanshan.bao@rice.edu)

Contents of this file

Figure S1 to S2

Additional Supporting Information

Movie S1 Evolution of the equatorial plane view of the ring current pressure, the ionospheric FAC, the ionospheric view of TEC and the equatorial plane mapping of the plasmapause and the TEC during the storm.

Movie S2 Evolution of the total electron content (TEC) and the plasmapause during the storm.

Movie S3 Evolution of the ring current and the plasmapause during the first period of southward interplanetary magnetic field (IMF).

Introduction

The supporting information contains two figures and two movies. Figure S1 shows the choices of the values of the contour lines in Figure 9 and 10 can describe the spatial distribution of the variables very well. It is reasonable to use the contour lines to represent the location of the plasmapause, ring current pressure, electron pressure, etc. Figure S2 shows Figure 3 from

"Plasmasphere response: Tutorial and review of recent imaging results" (Goldstein, 2006). It shows the observed spatial relationship between the storm-time plasmasphere and the partial ring current, which is similar to our simulation results as shown in Figure 10 and Movie S3.

Movie S1 - S3 are made from the simulation data with 2-miniute interval and 1-minute interval respectively. The simulation data has been converted into readable format for the Tecplot360 scientific visualization software. Movie S1-S2 are produced at 10fps and Movie S3 are produced at 20 fps in the MP4 format. Due to the limitation of the software, the time tag in the movies cannot be shown in HH:MM:SS format. It is counted in minutes from 16:00:00 UT 03-31-2001 when the simulation starts. The variable description in Movie S1 is the same as Figure 2. Movie S2 shows the plasmapause and TEC evolution from the beginning to the end of the storm main phase. The top left panel shows the equatorial plane view of the plasmapause (thick black contour line) and TEC color contour. The top right and lower panels show the ionospheric view of TEC in the SM coordinate and in the geographic coordinate respectively. The electric potential contours are plotted by thin black lines in all three panels, with dashed lines for negative values. Movie S3 shows the evolution of the ring current and the plasmapause during the first period of southward IMF. The electric fields transport both the ring current plasma and the plasmaspheric plume plasma toward the dayside. Since hot ions also follow the gradient and curvature drift, when the ring current particles penetrate to lower L shells, they overlap with the plasmapsheric plume near the dusk side. This process is consistent with the IMAGE satellite results as shown in Figure S2.

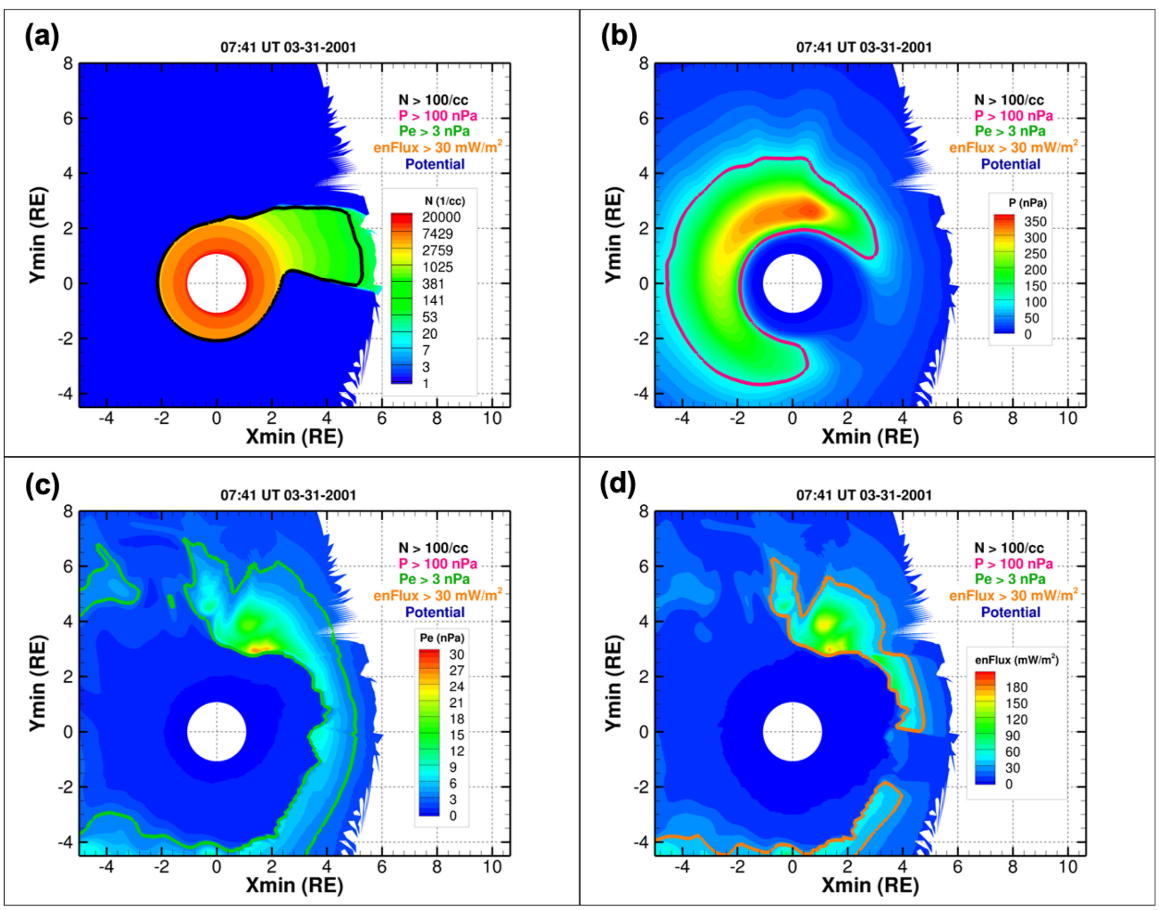

Figure S1. Colormap and corresponding color-coded contour lines used in Figure 10 and 11. The variables are (a) flux-tube-averaged plasmaspheric density, (b) plasma pressure, (c) electron pressure and (d) diffuse electron precipitation energy flux projected onto the equatorial plane. In each sub-figure, the physical quantity is mainly distributed inside the region enclosed by the contour line.

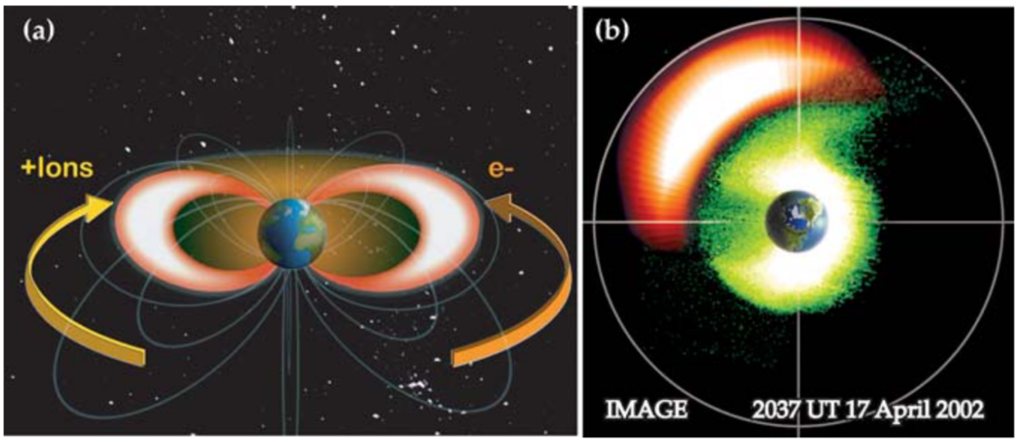

Figure 3. (a) Illustration of idealized ring current, format identical to that of Figure 1a. The ring current is the orange torus surrounding the Earth. Westward (eastward) magnetic drift of ions (electrons) indicated by the yellow (orange) curved arrow. (b) Global composite image of the inner magnetosphere (Pulkkinen *et al*., 2005). IMAGE HENA proton pressure (10–60 keV, 0.5–0.8 nPa) image has been overlaid onto Figure 1b. The HENA image shows the partial ring current that has been injected by a substorm. The plasmasphere and ring current are roughly spatially complementary, although there is some overlap near dusk, at the eastern edge of the plasmaspheric plume. (HENA image courtesy of P. C. Brandt; EUV image courtesy of B. R. Sandel).

Figure S2. Figure 3 of "Plasmasphere response: Tutorial and review of recent imaging results" (Goldstein, 2006) (b) shows the complementary shape of the plasmapause and the ring current in the composite image of the ring current (IMAGE HENA image in orange) and the plasmasphere (IMAGE EUV image in green). Spatial overlap between the ring current and the plasmaspheric plume is seen near the dusk side.

Movie S1 Evolution of the equatorial plane view of the ring current pressure, the ionospheric FAC, the ionospheric view of TEC and the equatorial plane mapping of the plasmapause and the TEC during the storm.
Movie S2 Evolution of the total electron content (TEC) and the plasmapause during the storm.
Movie S3 Evolution of the ring current and the plasmapause during the first period of southward interplanetary magnetic field (IMF).

Reference

Goldstein, J. Plasmasphere Response: Tutorial and Review of Recent Imaging Results. *Space Sci Rev* **124,** 203–216 (2006). https://doi.org/10.1007/s11214-006-9105-y